cmgh
CELLULAR AND MOLECULAR GASTROENTEROLOGY AND HEPATOLOGY

ORIGINAL RESEARCH

Ferroptosis Suppressor Protein 1 Inhibition Promotes Tumor Ferroptosis and Anti-tumor Immune Responses in Liver Cancer

Jacinth Wing-Sum Cheu,[1,*] Derek Lee,[1,*] Qidong Li,[1,*] Chi Ching Goh,[1] Macus Hao-Ran Bao,[1] Vincent Wai-Hin Yuen,[1] Misty Shuo Zhang,[1] Chunxue Yang,[1] Cerise Yuen-Ki Chan,[1] Aki Pui-Wah Tse,[1] Grace Fu-Wan Sit,[1] Cindy Xinqi Liu,[1] Irene Oi-Lin Ng,[1,2] Chun-Ming Wong,[1,2] and Carmen Chak-Lui Wong[1,2]

[1]Department of Pathology, Li Ka Shing Faculty of Medicine, The University of Hong Kong, Hong Kong; and [2]State Key Laboratory of Liver Research, The University of Hong Kong, Hong Kong

SUMMARY

Inhibition of ferroptosis suppressor protein 1 suppresses hepatocellular carcinoma tumor growth via the induction of ferroptosis. Ferroptotic cell death also promotes innate and adaptive anti-tumor immunity. This represents a novel and potent therapeutic target for hepatocellular carcinoma with improved treatment outcome.

BACKGROUND & AIMS: Hepatocellular carcinoma (HCC) is a highly aggressive malignancy with dreadful clinical outcome. Tyrosine kinase inhibitors and immune checkpoint inhibitors are the only United States Food and Drug Administration-approved therapeutic options for patients with advanced HCC with limited therapeutic success. Ferroptosis is a form of immunogenic and regulated cell death caused by chain reaction of iron-dependent lipid peroxidation. Coenzyme Q_{10} (CoQ_{10})/ferroptosis suppressor protein 1 (FSP1) axis was recently identified as a novel protective mechanism against ferroptosis. We would like to explore whether FSP1 could be a potential therapeutic target for HCC.

METHODS: FSP1 expression in human HCC and paired non-tumorous tissue samples were determined by reverse transcription-quantitative polymerase chain reaction, followed by clinicopathologic correlation and survival studies. Regulatory mechanism for FSP1 was determined using chromatin immunoprecipitation. The hydrodynamic tail vein injection model was used for HCC induction to evaluate the efficacy of FSP1 inhibitor (iFSP1) in vivo. Single-cell RNA sequencing revealed the immunomodulatory effects of iFSP1 treatment.

RESULTS: We showed that HCC cells greatly rely on the CoQ_{10}/FSP1 system to overcome ferroptosis. We found that FSP1 was significantly overexpressed in human HCC and is regulated by kelch-like ECH-associated protein 1/nuclear factor erythroid 2-related factor 2 pathway. FSP1 inhibitor iFSP1 effectively reduced HCC burden and profoundly increased immune infiltrates including dendritic cells, macrophages, and T cells. We also demonstrated that iFSP1 worked synergistically with immunotherapies to suppress HCC progression.

CONCLUSIONS: We identified FSP1 as a novel, vulnerable therapeutic target in HCC. The inhibition of FSP1 potently induced ferroptosis, which promoted innate and adaptive anti-tumor immune responses and effectively suppressed HCC tumor growth. FSP1 inhibition therefore represents a new therapeutic strategy for HCC. *(Cell Mol Gastroenterol Hepatol 2023;16:133–159; https://doi.org/10.1016/j.jcmgh.2023.03.001)*

Keywords: Hepatocellular Carcinoma; Immunogenic Cell Death; Lipid Peroxidation; Regulated Cell Death.

Hepatocellular carcinoma (HCC) is the most common form of primary liver cancer that originates from hepatocytes. Late symptom presentations result in most patients with HCC diagnosed at advanced stages, and curative treatments like surgical resection are unfeasible.[1] Effective therapeutic options for patients with HCC are limited, as HCC is highly recurrent and highly resistant to conventional chemo- and radiotherapy. Currently, tyrosine kinase inhibitors (TKIs) (sorafenib, lenvatinib, regorafenib,

*Authors share co-first authorship.

Abbreviations used in this paper: 4-HNE, 4-hydroxynonenal; Afp, alpha fetoprotein; AKR1B10, aldo-keto reductase family 1 member B10; AKR1C1, aldo-keto reductase family 1 member C1; APC, antigen presenting cell; ARE, antioxidant response element; BMM, bone marrow-derived macrophage; BrdU, bromodeoxyuridine; CDDO-Im, CDDO-Imidazolide; ChIP, chromatin immunoprecipitation; CoQ, coenzyme Q; CTV, cell-trace violet; DAMPs, damage-associated molecular patterns; DC, dendritic cell; FBS, fetal bovine serum; FSP1, ferroptosis suppressor protein 1; GPX4, glutathione peroxidase 4; GSH, glutathione; HCC, hepatocellular carcinoma; HDTVi, hydrodynamic tail vein injection; HFD, high-fat diet; ICD, immunogenic cell death; ICI, immune checkpoint inhibitor; iFSP1, FSP1 inhibitor; KEAP1, kelch-like ECH-associated protein 1; LC-MS, liquid chromatography-mass spectrometry; LDH, lactate dehydrogenase; MAF, MAF BZIP transcription factor; MDA, malondialdehyde; ME1, malic enzyme 1; MTHFD1L, methylenetetrahydrofolate dehydrogenase 1-like; MUT, mutant; NQO1, NAD(P)H dehydrogenase, quinone 1; NRF2, nuclear factor erythroid 2-related factor 2; NT, non-tumorous; NTC, non-targeting control; PBS, phosphate buffered saline; PL-PUFA-OOH, phospholipid hydroperoxides; P/S, penicillin-streptomycin; PUFA, polyunsaturated fatty acid; RCD, regulated cell death; ROS, reactive oxygen species; RT-qPCR, real-time quantitative polymerase chain reaction; scRNA-seq, single-cell RNA sequencing; SD, standard deviation; SFN, L-sulphoraphane; shRNA, short hairpin RNA; TAM, tumor-associated macrophage; TCGA, The Cancer Genome Atlas; TF, transferrin; TKI, tyrosine kinase inhibitor; TKT, transketolase; tSNE, t-distributed stochastic neighbor embedding; WT, wild-type.

Most current article

2352-345X
https://doi.org/10.1016/j.jcmgh.2023.03.001

cabozantinib) and immune checkpoint inhibitors (ICIs) (nivolumab [anti-PD-1] and atezolizumab [anti-PD-L1]) are the only United States Food and Drug Administration-approved drugs for patients with advanced HCC.[2] Unfortunately, TKIs provide modest survival benefits, whereas ICIs are only effective in a small subset of patients with HCC. Drugs that can target HCC cells to cell death are worth investigation. Further investigation into drugs that can induce HCC cell death will benefit the development of effective HCC treatment, as these agents may be utilized as HCC therapeutics.

Ferroptosis is the most-recently discovered form of regulated cell death (RCD) that aggravates degenerative diseases and paradoxically suppresses cancer cell growth.[3,4] Ferroptosis vastly differs from conventional forms of RCDs. Morphologically, ferroptosis displays outer mitochondrial membrane rupture, shrunken mitochondria with condensed membrane densities, and loss of cristae.[5] Biochemically, ferroptosis is dependent on excessive iron-mediated lipid peroxidation.[6] Iron reacts with hydrogen peroxides to generate hydroxyl radicals, highly toxic reactive oxygen species (ROS) that further react with polyunsaturated fatty acid (PUFA) tails on the cell membrane lipid bilayer to generate lipid peroxides, a process called lipid peroxidation. Lipid peroxides establish a chain reaction and produce more lipid peroxides. These further cause damage to the cell membrane, which eventually causes ferroptosis. Iron is essential for lipid peroxidation chain reaction propagation and also for catalyzing iron-dependent enzymes like lipoxygenases to generate lipid peroxides.[7] Iron is transported from the blood into cells by transferrin (TF), stored in ferritin, and released upon ferritinophagy, an autophagic degradation process of ferritin (Figure 1*A*).[8-10] Cells have 3 major protective mechanisms against ferroptosis: (1) the cysteine/glutathione (GSH)/glutathione peroxidase 4 (GPX4) pathway; (2) the mitochondrial GPX4-dependent coenzyme Q (CoQ)/dihydroorotate dehydrogenase (DHODH) pathway; and (3) the CoQ_{10}/ferroptosis suppressor protein 1 (FSP1) pathway. The cysteine/GSH/GPX4 pathway was the first discovered and most well-known protective pathway against ferroptosis.[11] In cysteine/GSH/GPX4 pathway, GPX4 removes phospholipid peroxides using reduced GSH. GSH synthesis depends on the xCT cystine-glutamate antiporter (encoded by SLC7A11 and SLC3A2), which pumps cystine into cells in exchange for glutamate.[5] GPX4 reduces phospholipid hydroperoxides (PL-PUFA-OOH) to counteract ferroptosis. Dihydroorotate dehydrogenase is a mitochondrial enzyme localized on the outer face of the inner membrane. It converts dihydroorotate to orotate and generates $FMNH_2$ to reduce ubiquinone (CoQ) into ubiquinol ($CoQH_2$) to protect cells from ferroptosis at the mitochondrial membrane.[12] The most common form of CoQ in human is CoQ_{10}.[13] In the CoQ_{10}/FSP1 pathway, FSP1, a CoQ oxidoreductase, converts CoQ to $CoQH_2$ to stabilize PL-PUFA-OOH.[14,15] The N-terminal myristylation of FSP1 localizes FSP1 to cell membrane, which aids PL-PUFA-OOH removal.[14,15] The CoQ_{10}/FSP1 pathway acts independently of GPX4 as FSP1 does not affect the xCT antiporter and cysteine transport, GSH levels, and total PL-PUFA (Figure 1*A*). Although the GPX4 pathway is an attractive therapeutic target for cancer treatment through ferroptosis induction, the efficacy of current GPX4 inhibitors is limited to in vitro studies, and the responses vary across different cancer cell lines.[16] Inhibitors, such as erastin and sorafenib, that target xCT antiporter are not highly specific. GPX4 is expressed in T cells, and these inhibitors could therefore inhibit T cells and cause T cell exhaustion in the cancer context.[17] These limitations prompted us to explore new anti-ferroptotic mechanisms beyond the cysteine/GSH/GPX4 pathway to discover new therapeutic strategies against HCC. The CoQ_{10}/FSP1 pathway is another protective pathway against ferroptosis that works independently of the cysteine/GSH/GPX4 pathway.[14,15] A potent FSP1 inhibitor, iFSP1, was identified. iFSP1 induced ferroptosis and suppressed cancer cell growth in vitro with GPX4 inhibited. The in vivo efficacy of iFSP1 is yet to be investigated.[15]

Immunogenic cell death (ICD) is characterized by its release or membrane exposure of damage-associated molecular patterns (DAMPs), which recruit and activate innate immune cells, subsequently eliciting adaptive immune responses.[18,19] Innate immune cells play a key role in ICD-elicited anti-tumor immune responses. Dendritic cells (DCs) internalize dying cells or cellular fragments for presenting tumor-associated antigens to T cells via major histocompatibility complex molecules.[20] Macrophages engulf dying cells and mediate the removal of cancer cells, accompanied by the production of pro-inflammatory cytokines.[21] The immunomodulatory roles of ferroptotic cells in HCC are yet to be explored. Apart from activating innate immune cells through ICD induction, a new generation of immunotherapies that target innate immune cells has emerged as a promising therapeutic approach. Among these is CD40 agonist. CD40 is a co-stimulatory receptor expressed on antigen presenting cells (APCs), such as macrophages and DCs. Ligation of CD40 with CD40L expressed on activated T cells enhances antigen presentation by macrophages and DCs.[22] CD40 agonist was shown to suppress tumor growth by enhancing major histocompatibility complex and co-stimulatory molecule expression on DCs[23] and reprogramming tumor-associated macrophage (TAM).[24,25] Here, we explore whether CD40 agonist can further activate innate immune cells and enhance iFSP1 efficacy in HCC.

We hypothesize that targeting FSP1 induces ferroptosis in cancer cells and promotes anti-tumor immune responses. Here, we showed that targeting FSP1 alone is sufficient to severely induce ferroptosis and suppress HCC cells proliferation as well as HCC tumor growth even with intact GPX4. Our work suggested that perturbation of the CoQ_{10}/FSP1 pathway suffices to inhibit HCC development through ferroptosis induction. More excitingly, we unprecedentedly showed that iFSP1 treatment in mice profoundly increased the number of DCs, macrophages, and T cells in the tumors and suggested that iFSP1 works in synergy with multiple immunotherapies to improve the survival of mice with HCC.

Results

FSP1 Overexpression is Significantly Associated With Human HCC

To understand the clinical significance of ferroptosis regulation, especially FSP1 in human HCC, we made use of

transcriptome sequencing results from 49 paired human HCC/non-tumorous (NT) liver tissue samples from The Cancer Genome Atlas (TCGA). Significant overexpression of FSP1 was found in human HCC tissues compared with NT tissues (Figure 1*B*). These transcriptome sequencing results also revealed significant downregulation of pro-ferroptotic

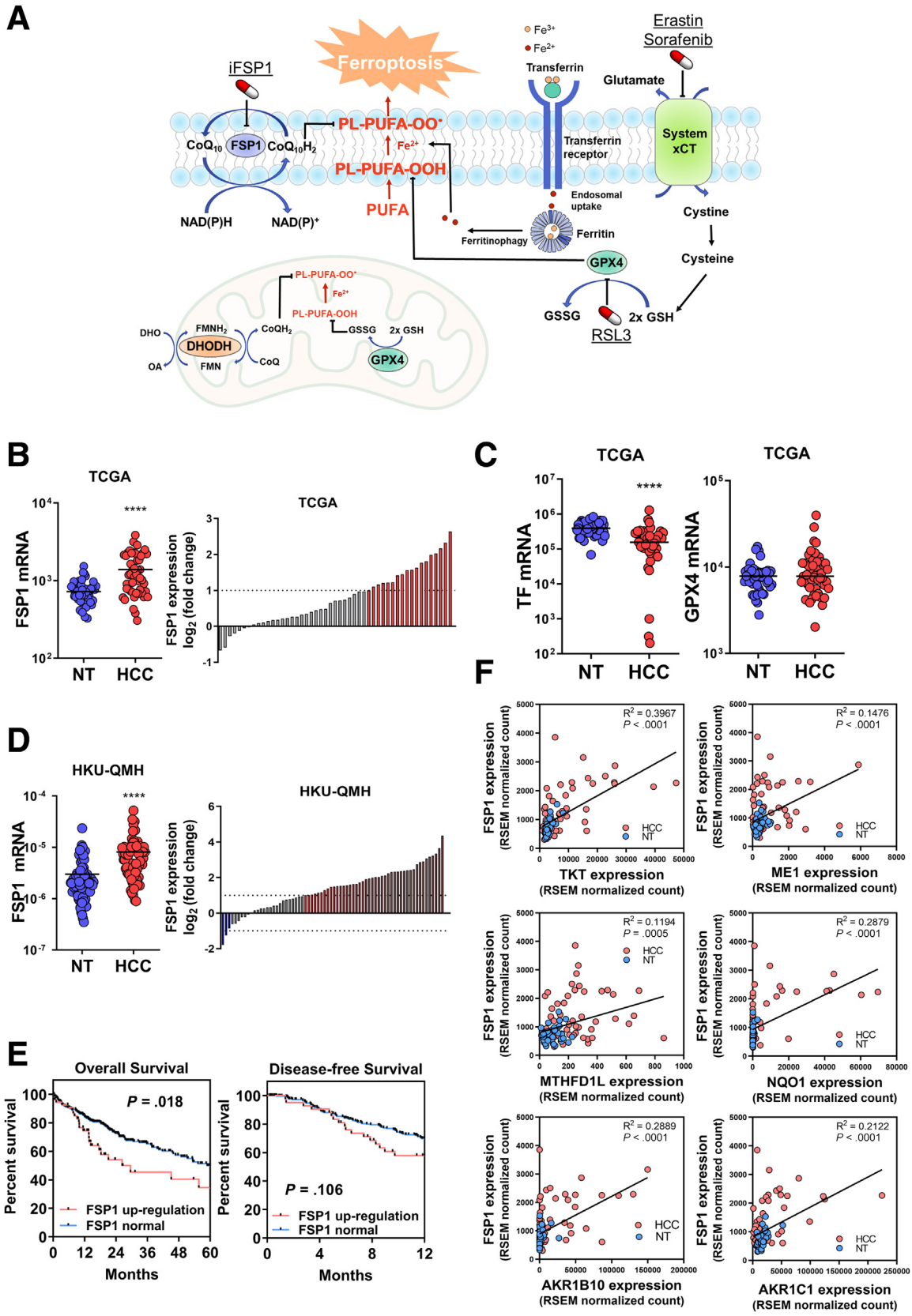

Table 1. Clinicopathological Correlation of FSP1 Overexpression in Human HCC

Clinicopathological phenotype	Number of cases	Mean	*P*-value
Cellular differentiation by Edmonson grading			
I–III	23	0.43	.101
IV–VI	40	0.23	
Chronic liver disease			
Normal	12	0.25	.638
Chronic hepatitis and cirrhosis	53	0.32	
Direct liver invasion			
Absent	24	0.29	.726
Present	36	0.25	
Hepatitis B surface antigen by IHC			
Absent	16	0.25	.511
Present	44	0.34	
Hepatitis C surface antigen by IHC			
Absent	13	0.38	.018[a]
Present	21	0.00	
Plasma hepatitis B surface antigen			
Absent	9	0.33	.718
Present	40	0.40	
pTNM stage			
I/II	30	0.30	.718
I/II/III/IV	32	0.34	
Tumor encapsulation			
Absent	27	0.41	.440
Present	17	0.53	
Tumor microsatellite formation			
Absent	25	0.36	.550
Present	35	0.29	
Tumor size			
$\leq$ 5 cm	33	0.18	**.021**[a]
$>$ 5 cm	31	0.45	
Venous invasion			
Absent	19	0.47	.829
Present	25	0.44	

Note: Mean: average values of FSP1 expression in human HCC samples relative to its paired NT tissues determined with the formula: $\Delta Ct^{HCC(FSP1\text{-}18S)} - \Delta Ct^{NT(FSP1\text{-}18S)}$.
Note: Boldface *P* values indicate statistical significance.
FSP1, Ferroptosis suppressor protein 1; HCC, hepatocellular carcinoma; IHC, immunohistochemistry; NT, non-tumorous; pTNM, pathological tumor-node-metastasis.
[a]*T* test: $P < .05$.

gene TF (Figure 1*C*). Interestingly, genes from the classic cysteine/glutathione/GPX4 anti-ferroptosis pathway, including GPX4, a major anti-ferroptotic gene, were not upregulated in human HCC (Figure 1*C*). This suggested that HCC was protected from ferroptosis by limiting iron uptake into cancer cells and upregulation of FSP1 pathway but not GPX4 pathway, as both pathways work independently to counteract ferroptosis. An expanded cohort of 70 HCC cases from our institute (HKU-QMH) also demonstrated FSP1 overexpression in HCC tissues over NT liver tissues at the mRNA level determined by real-time quantitative polymerase chain reaction (RT-qPCR). FSP1 overexpression by at

Figure 1. (***See previous page***). **FSP1 is overexpressed in human HCC.** (*A*) Schematic representation of pathways involved in ferroptosis regulation. (*B*) *Left:* TCGA data revealed upregulation of FSP1 in 49 human HCC tissues compared with corresponding NT liver tissues. *Right:* Waterfall plot showed upregulation of FSP1 in 37% (18/49) of patients with HCC retrieved from TCGA by at least 2-fold. (*C*) *Left*: TCGA data revealed downregulation of TF in human HCC tissues compared with corresponding NT liver tissues. *Right*: TCGA data revealed GPX4 is not upregulated in human HCC tissues compared with corresponding NT liver tissues. (*D*) *Left*: RT-qPCR results from an expanded cohort of 70 human HCC tissues from our institute demonstrated upregulation of FSP1 compared to corresponding NT liver tissues. *Right:* Waterfall plot showed upregulation of FSP1 in 63% (44/70) of patients with HCC by at least 2-fold. (*E*) Analysis of TCGA data revealed patients with HCC with FSP1 upregulation (Z-score $>$ 1) are associated with poorer overall and disease-free survival. (*F*) TCGA data revealed positive correlations between expression of FSP1 with expressions of known NRF2-targeted genes including TKT, ME1, MTHFD1L, NQO1, AKR1B10, and AKR1C1 in human HCC and NT liver tissues. ****$P < .0001$ vs NT. *B–D, F*: Student *t* test. *E*: Kaplan-Meier followed by log-rank test. RSEM = RNA-Seq expression estimation by expectation maximization.

least 2-fold was found in 44 of 70 (62.9%) of the HCC tumor samples (Figure 1*D*). Clinicopathologically, FSP1 overexpression in HCC samples from our institute were significantly associated with patients with HCC with larger tumor size (>5 cm) (Table 1). Moreover, TCGA data indicated patients with HCC with higher FSP1 expression were significantly correlated with poorer overall survival ($P = .018$) and were associated with poorer disease-free survival ($P = .106$) (Figure 1*E*). Interestingly, we found positive correlation between mRNA expression of FSP1 and nuclear factor erythroid 2-related factor 2 (NRF2), transcriptional targets we previously identified, including transketolase (TKT), malic enzyme 1 (ME1), and methylenetetrahydrofolate dehydrogenase 1-like (MTHFD1L), as well as other well-known NRF2 targets NAD(P)H dehydrogenase, quinone 1 (NQO1), aldo-keto reductase family 1 member B10 (AKR1B10), and aldo-keto reductase family 1 member C1 (AKR1C1) in human HCC and NT liver tissues from TCGA (Figure 1*F*).[26-28] Expression analyses from clinical HCC samples on TCGA and our institute converged to identify overexpression of FSP1 in human HCC is significantly correlated with dismal clinicopathological features of HCC.

FSP1 is Regulated by the KEAP1/NRF2 Pathway

Next, we aimed to understand the regulatory mechanism that drives the overexpression of FSP1 in human HCC. Because FSP1 is essential for counteracting lipid peroxidation, it was postulated that FSP1 expression is regulated by the kelch-like ECH-associated protein 1 (KEAP1)/NRF2 pathway like other oxidative stress-related genes. KEAP1/NRF2 is the master regulatory pathway for an array of genes known for protection against oxidative stress.[29] We found positive correlation between FSP1 expression with NRF2 transcriptional targets we previously found, including TKT, ME1, MTHFD1L, and known NRF2 targets NQO1, AKR1B10, and AKR1C1 (Figure 1*F*), strongly suggesting that FSP1 overexpression in human HCC is regulated by the KEAP1/NRF2 pathway (Figure 2*A*).[26-28] Oxidative stress is a common feature in solid tumors and is believed to promote FSP1 upregulation in human HCC. In silico analysis identified a putative antioxidant response element (ARE) at −22 bp upstream of the transcription start site in FSP1. Furthermore, dramatic enrichment of NRF2 binding at the mapped putative ARE of FSP1 was confirmed by chromatin immunoprecipitation (ChIP) assay using NRF2 and IgG antibodies on multiple HCC cell lines, including MHCC97L, PLC/PRF/5, and Huh7 (Figure 2*B*). We next sought to confirm the regulatory role of KEAP1/NRF2 and small Maf proteins that dimerize with NRF2 to bind to ARE sequences on FSP1. Stable NRF2, KEAP1, and MAF BZIP transcription factor (MAF) knockdown clones were established in multiple HCC cell lines, including MHCC97L, PLC/PRF/5, and Huh7 using short hairpin RNAs (shRNAs) (shNRF2, shKEAP1, and shMAF). To show that the ARE we identified at FSP1 promoter region is functional and how NRF2 and MAF regulates FSP1, we performed luciferase reporter assay. Wild-type (WT) and mutated (MUT) AREs were first inserted into pGL4 luciferase reporter vector, and we transfected stable NRF2 and MAF knockdown clones of Huh7 with the WT-ARE or MUT-ARE containing luciferase plasmids. We then exposed the cells to treatment of tert-Butyl hydroperoxide (tBHP; Sigma-Aldrich, St. Louis, MO), an oxidant to induce NRF2, and determined the FSP1 promoter luciferase activities. We showed that tBHP treatment induced luciferase activities in cells expressing WT-ARE but not the MUT one (Figure 2*C*). The induction of promoter activities by tBHP in WT-ARE expressing cells could be abrogated by NRF2 or MAF knockdown (Figure 2*C*). We previously demonstrated the NRF2 stable knockdown clones down-regulated the expressions of known NRF2-target genes like TXNRD1 and ME1, whereas KEAP1 stable knockdown clones up-regulated the same targets.[27,30] These results validate the validity of the NRF2 and KEAP1 inhibitions, and, consistent with our hypothesis, NRF2 inhibition effectively down-regulated FSP1 expressions (Figure 2*D*) and inhibition of KEAP1, the NRF2 suppressor, effectively up-regulated FSP1 expressions (Figure 2*E*) at both the mRNA and protein levels. We also confirmed that MAF contributes to FSP1 regulation in stable MAF knockdown clones. The inhibition of MAF effectively down-regulated FSP1 expression at the mRNA level (Figure 3*A*). Finally, we made use of a chemical NRF2 inducer L-sulforaphane (SFN; Sigma-Aldrich) and treated HCC cells (MHCC97L, PLC/PRF/5, Huh7) at various concentrations. Dose-dependent up-regulation of FSP1 were consistently observed at mRNA and protein levels upon SFN treatment across all 3 HCC cell lines (Figure 2*F*). We further confirmed our findings using another NRF2 inducer CDDO-Imidazolide (CDDO-Im; Tocris Bioscience, Bristol, UK), as dose-dependent up-regulation of FSP1 was also observed at the mRNA level across different HCC cells upon CDDO-Im treatment (Figure 3*B*). Taken together, in silico analysis, ChIP assay, luciferase reporter assay, and NRF2 inhibition strongly suggested that FSP1 is transcriptionally regulated by NRF2 in HCC.

Knockdown of FSP1 Resulted in Ferroptosis-induced HCC Cell Death

We next studied the functional roles of FSP1 in human HCC, and we performed loss-of-function studies. First, stable FSP1 knockdown clones were established in MHCC97L cells with 2 independent shRNA sequences (shFSP1-23, -24). Significant inhibition of FSP1 expressions compared with non-targeting control (NTC) were evident in mRNA and protein levels (Figure 4*A*). FSP1 is an oxidoreductase, converting oxidized CoQ_{10} into reduced $CoQ_{10}H_2$. Liquid chromatography-mass spectrometry (LC-MS) confirmed that knockdown of FSP1 significantly reduced intracellular $CoQ_{10}H_2/CoQ_{10}$ ratio (Figure 4*B*). Through the reduction of CoQ_{10}, FSP1 is important for lipid peroxidation prevention, and we detected significant increase in intracellular lipid peroxidation in MHCC97L cells upon FSP1 knockdown (shFSP1-23, -24) compared with NTC control cells using BODIPY 581/591 C_{11} staining (Invitrogen, Carlsbad, CA) (Figure 4*C*). FSP1 knockdown obstructed HCC cell growth

in vitro as cell proliferation rates of both knockdown clones (shFSP1-23, -24) were significantly lower than NTC cells. The reduced cell proliferation rates of the FSP1 knockdown clones were rescued upon treatment of ferroptosis inhibitor ferrostatin-1 (Fer-1; Sigma-Aldrich) (Figure 4*D*). This suggested that FSP1 knockdown adversely affects HCC growth

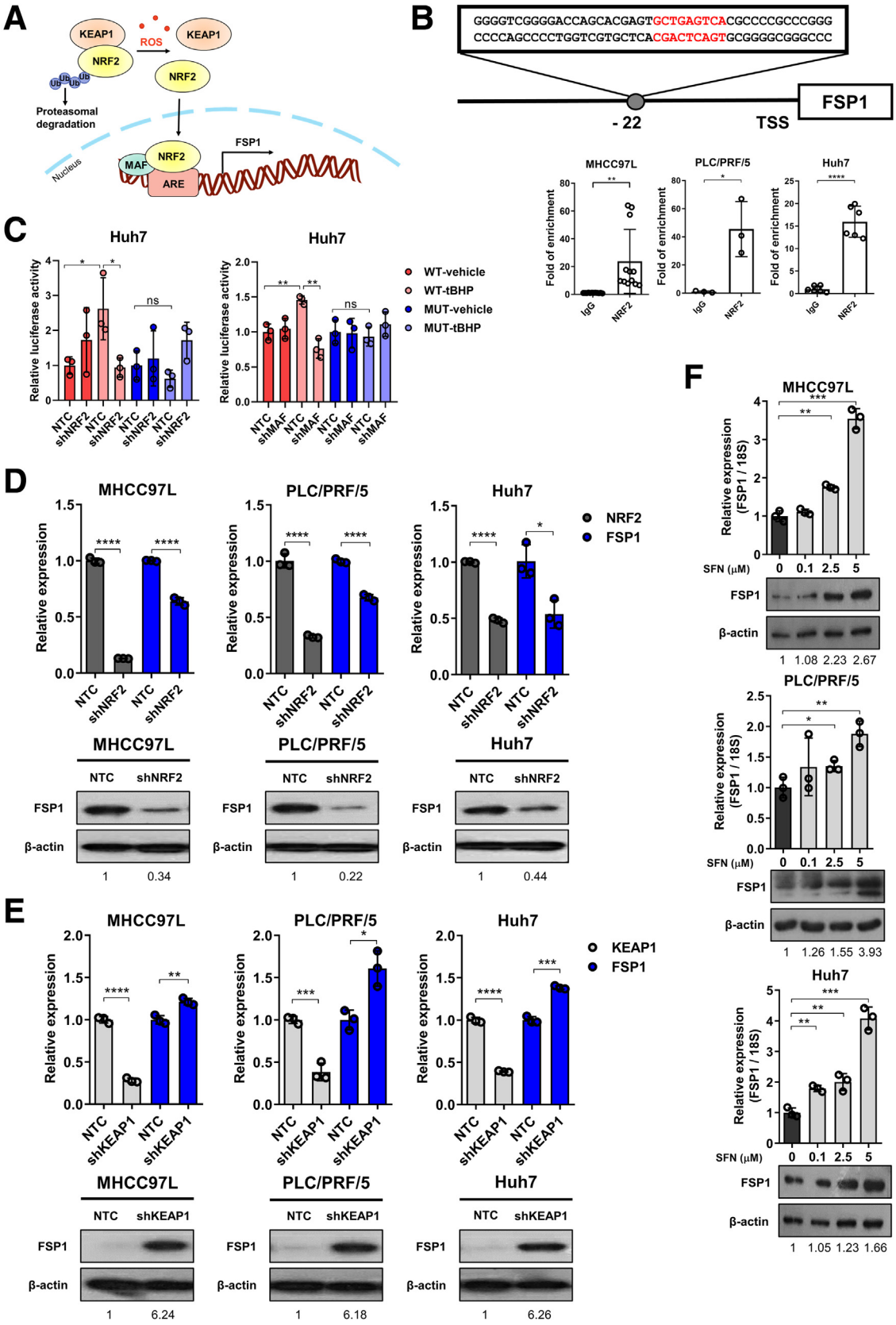

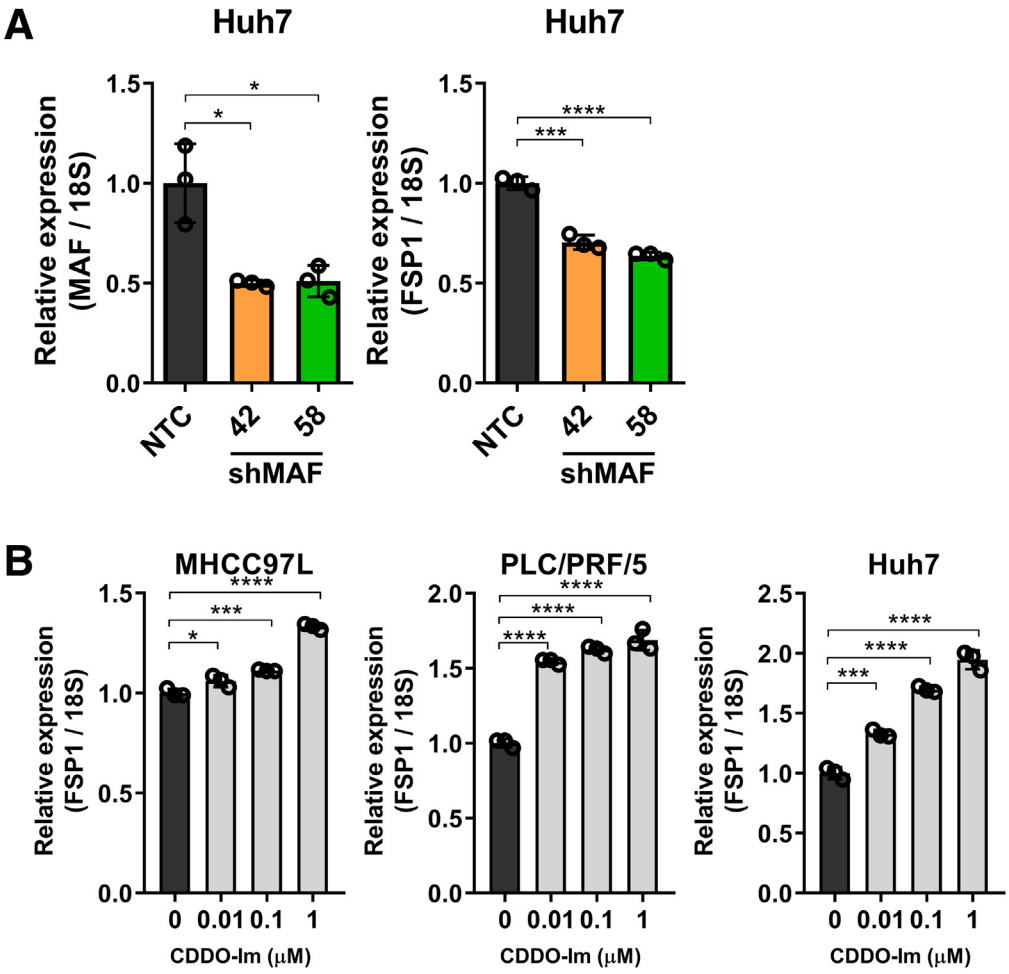

Figure 3. FSP1 is regulated by NRF2 and MAF in human HCC. (*A*) *Left:* Knockdown of MAF in Huh7 cells is confirmed by RT-qPCR. *Right:* Knockdown of MAF in Huh7 cells significantly downregulated FSP1 expressions at mRNA level as confirmed by RT-qPCR. (*B*) Activation of NRF2 upon treatments of 0.01, 0.1, 1 μM NRF2 activator CDDO-Im resulted in dose-dependent upregulation of FSP1 mRNA expressions in MHCC97L, PLC/PRF/5, and Huh7 cells as confirmed by RT-qPCR. *$P < .05$, ***$P < .001$, ****$P < .0001$ vs NTC or 0 μM as indicated. Error bars indicate mean ± SD. Student *t* test.

through lipid peroxidation-mediated ferroptosis. Luciferase-labeled MHCC97L stable FSP1 knockdown clones and NTC were orthotopically injected into nude mice livers. Tumor volume and bioluminescent measurements consistently revealed that smaller HCC tumors were derived from FSP1 knockdown clones. Moreover, lung tissue imaging ex vivo revealed FSP1 knockdown suppressed the growth of lung metastases (Figure 4*E*). To confirm that FSP1 is essential for preventing ferroptosis-induced HCC cell death, we confirmed that FSP1 inhibition resulted in the accumulation of intracellular lipid peroxidation. A significant increase in intracellular levels of lipid peroxidation by-products 4-hydroxynonenal (4-HNE) and malondialdehyde (MDA) were detected from FSP1 knockdown stable clones relative to NTC (Figure 4*F*). We then examined whether cytotoxic effects were elicited because of lipid peroxidation. Quantification of lactate dehydrogenase (LDH) released from damaged cells, an indicator of cell death, revealed that FSP1 knockdown cells released significantly higher levels of LDH compared with NTC (Figure 4*G*). Furthermore, SYTOX Green

Figure 2. (***See previous page***). **FSP1 is regulated by NRF2 in human HCC.** (*A*) Schematic representation of FSP1 regulation mediated by the KEAP1/NRF2 pathway. (*B*) *Top:* ARE was located at -22 bp upstream of the transcription start site (TSS) of FSP1. *Bottom:* ChIP assay on HCC cells including MHCC97L, PLC/PRF/5, and Huh7 using NRF2, and IgG antibodies demonstrated specific and dramatic enrichment of NRF2 at the identified putative ARE of FSP1. (*C*) *Left:* Luciferase reporter assay showed that tert-Butyl Hydroperoxide (tBHP) treatment induced luciferase activities in Huh7 cells transfected with luciferase plasmid containing WT ARE we identified but not those with MUT ARE or knockdown of NRF2. *Right:* Luciferase reporter assay showed that tBHP-induced luciferase activities in Huh7 cells expressing WT ARE were abrogated upon knockdown of MAF. (*D*) Knockdown of NRF2 in MHCC97L, PLC/PRF/5, and Huh7 cells significantly downregulated FSP1 expressions at mRNA and protein levels confirmed by RT-qPCR and Western blotting, respectively. (*E*) Knockdown of KEAP1 in MHCC97L, PLC/PRF/5, and Huh7 cells significantly upregulated FSP1 expressions at mRNA and protein levels confirmed by RT-qPCR and Western blotting, respectively. (*F*) Activation of NRF2 upon treatments of 0.1, 2.5, 5 μM NRF2 activator SFN resulted in dose-dependent upregulation of FSP1 mRNA and protein expressions in MHCC97L, PLC/PRF/5, and Huh7 cells as confirmed by RT-qPCR and Western blotting, respectively. Error bars indicate mean ± SD. *$P < .05$, **$P < .01$, ***$P < .001$, ****$P < .0001$ vs IgG, NTC, or 0 μM as indicated. Student *t* test.

dead cell staining (Invitrogen) also demonstrated similar results as LDH release. Fer-1 treatment to FSP1 knockdown clones (shFSP1-23, -24) significantly lowered the relative SYTOX Green staining compared with untreated cells (Figure 4*H*). Fer-1 treatment was also found to significantly increase relative bromodeoxyuridine (BrdU) intensities in MHCC97L-shFSP1-23 and -24 cells. Treatment of inhibitors of other forms of RCDs including necroptosis (GSK'872), apoptosis (Z-VAD-FMK), and autophagy (MRT68921), however, did not rescue the suppressed cell proliferation rates in FSP1 stable knockdown HCC cells (Figure 4*I*). The observations altogether demonstrated that only ferroptosis inhibitor (eg, Fer-1) was able to rescue FSP1 knockdown-induced cell death in HCC cells. This indicated the

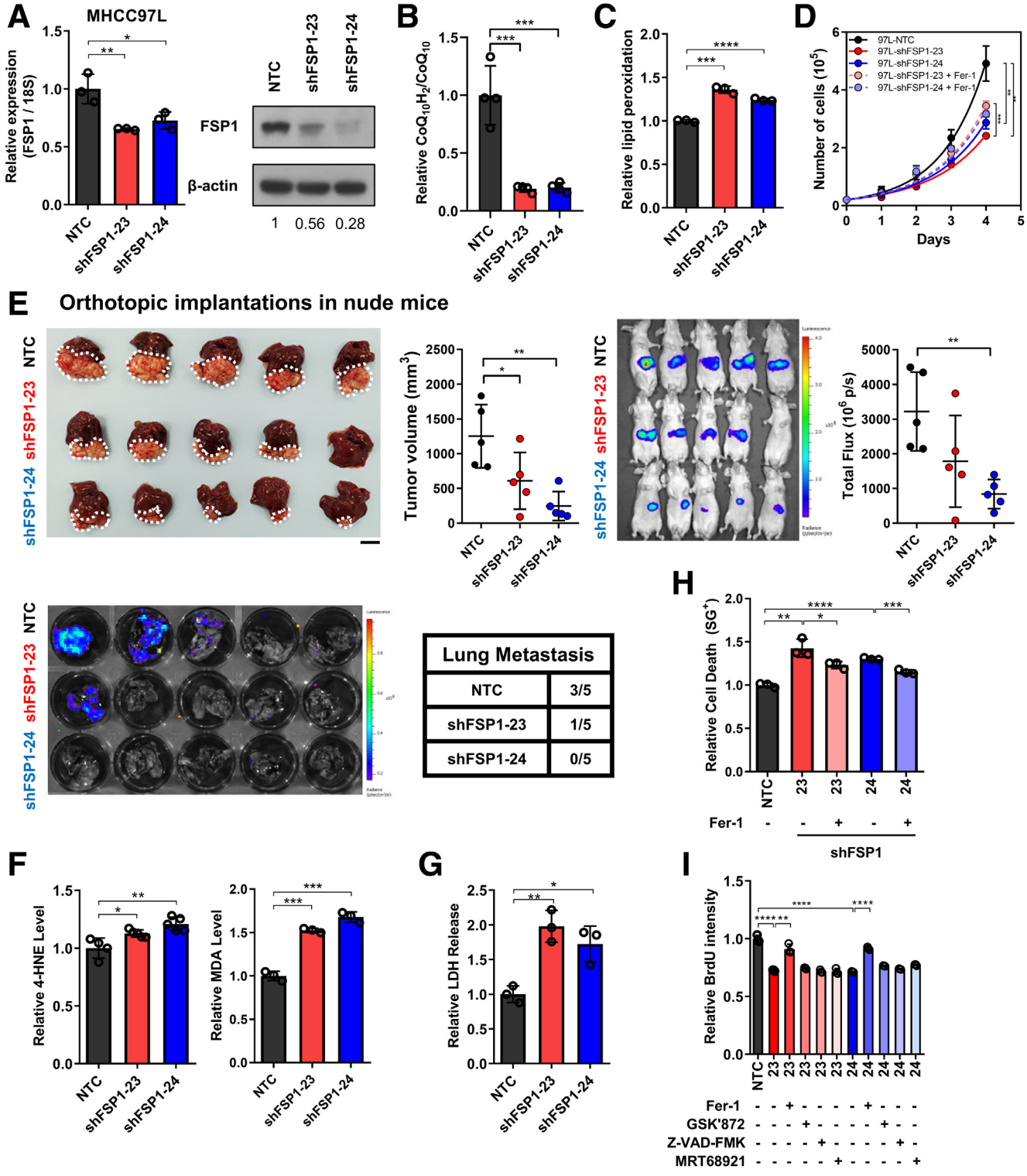

important role of FSP1 for the protection of HCC cells from ferroptosis and cell death.

iFSP1 Effectively Induced HCC Cell Death Via Immune Cell Recruitment

We demonstrated that FSP1 knockdown led to accumulation of intracellular lipid peroxidation, which ultimately resulted in ferroptosis-induced cell death in human HCC. As we now look to translate this concept for clinical application, we made use of a specific chemical FSP1 inhibitor, iFSP1.[15] As a novel and sole FSP1 inhibitor, we tested the effects of iFSP1 on MHCC97L cells at multiple concentrations. Cell proliferation rates were significantly suppressed dose-dependently upon iFSP1 treatment (Figure 5*A*). Additionally, iFSP1 treatment, like erastin, which targets the xCT antiporter of the GPX4 system, also induced a greater extracellular release of LDH compared with vehicle control, further indicating that iFSP1 elicited cytotoxic effects on HCC cells (Figure 5*B*). Treatment of iFSP1 with the same concentrations as Figure 5*A* also displayed dose-dependent increase of intracellular lipid peroxidation with BODIPY 581/591 C_{11} staining, and cell death indicated by increased SYTOX Green dead cell staining (Figure 5*C*–*D*). These results together suggested that pharmacological inhibition of FSP1 using iFSP1 effectively induces ferroptosis, which inhibits HCC growth. We then performed in vitro assays to detect the intracellular levels of lipid peroxidation by-products 4-HNE and MDA in HCC cells upon iFSP1 treatment. Both 4-HNE and MDA levels were significantly increased upon iFSP1 treatment relative to vehicle control cells (Figure 5*E*). Upon iFSP1 treatment in MHCC97L cells, we observed that co-treatment of Fer-1 reversed the effects as the relative BrdU intensities significantly increased. Co-treatment of necroptosis (GSK'872), apoptosis (Z-VAD-FMK), and autophagy (MRT68921) inhibitors had minimal rescue effect to the suppressed cell proliferation induced by iFSP1 in the BrdU assay (Figure 5*F*). Dying cells recruit APCs and phagocytes that mediate their clearance. We then asked whether iFSP1 treatment promotes HCC cells to be phagocytosed by macrophages. We first pre-treated mouse HCC cells Hepa1-6 with iFSP1 or vehicle control and labeled them with CellTrace Violet (CTV) dye (Invitrogen). Then, we co-cultured CTV-labeled Hepa1-6 cells with murine bone marrow-derived macrophages (BMMs). Phagocytic events were measured by CTV^+ cells in $CD11b^+$ $F4/80^+$ macrophage population using flow cytometry (Figure 5*Gi*). We showed that iFSP1 treatment significantly enhanced phagocytosis of Hepa1-6 cells by BMMs (Figure 5*Gii*). Co-treatment with iFSP1 and Fer-1 abrogated the increase of phagocytosis of Hepa1-6 cells by BMMs (Figure 5*Giii*). We have demonstrated that ferroptotic HCC cells recruit macrophages and enhance the engulfment of ferroptotic cells, suggesting the potential immunomodulatory effect of iFSP1. To further study the therapeutic potential of iFSP1 and whether it affects the intra-tumoral immune composition, we induced HCC tumor with $Keap1^{KO}$/c-Myc^{OE} genetic background by hydrodynamic tail vein injections (HDTVi) in immunocompetent C57BL/6N mice fed with high-fat diet (HFD) (60 kcal% fat, 0.1% methionine, no choline) (Research Diets, Inc, New Brunswick, NJ). In this model, HFD promoted lipid accumulation in liver, whereas $Keap1^{KO}$ resulted in Nrf2 activation, generating a highly aggressive murine HCC model (Figure 6). To characterize this model, we performed hematoxylin and eosin staining on the tumors, and they were confirmed to be HCC (Figure 7*A*). We showed that FSP1 expression was particularly induced in $Keap1^{KO}$ tumors (Figure 7*B*). Furthermore, conventional HCC marker alpha fetoprotein (Afp) was overexpressed in tumor tissues (Figure 7*C*). We showed that iFSP1 treatment significantly suppressed HCC tumor growth with no adverse effects on body weight (Figure 5*Hi*). Furthermore, flow cytometry analysis illustrated that iFSP1 greatly increased the number of macrophages, DCs, and $CD4^+$ and $CD8^+$ T cells in HCC tumor compared with vehicle control (Figure 5*Hii*). We observed no change in the number of neutrophils and a slight increase in monocytes (Figure 7*D*). Further characterizations showed that iFSP1 promoted tumor infiltration of M1 macrophages and effector T cells but no change in M2 macrophages (Figure 7*D*–*E*). Tumor infiltration of $CD4^+$ and $CD8^+$ T cells was confirmed by immunohistochemical (IHC) staining (Figure 5*I*).

Figure 4. (***See previous page***). **FSP1 knockdown induced ferroptotic HCC cell death.** (*A*) Stable FSP1-knockdown subclones (shFSP1) were established using shRNAs. RT-qPCR and Western blotting confirmed the knockdown efficiencies at mRNA and protein levels, respectively. (*B*) LC-MS demonstrated decrease in relative $CoQ_{10}H_2/CoQ_{10}$ ratio in MHCC97L-shFSP1 cells. (*C*) BODIPY 581/591 C_{11} staining in MHCC97L-shFSP1 cells revealed a significant increase in lipid peroxidation. (*D*) Cell proliferation rates of MHCC97L-NTC and -shFSP1 cells by cell counting daily revealed that FSP1 knockdown significantly suppressed HCC cell growth. Suppressed growth rates were rescued using ferroptosis inhibitor Fer-1. (*E*) Orthotopic implantation of luciferase-labeled MHCC97L-NTC and MHCC97L-shFSP1-23, and MHCC97L-shFSP1-24 cells into the livers of nude mice (n = 5 mice per experimental group) revealed that FSP1 knockdown suppressed HCC tumor formation in vivo. *Top, left:* Representative picture of orthotopic xenografts and quantification of tumor volume. *Top, right:* Bioluminescent images of mice implanted with different stable subclones. *Bottom:* Bioluminescent images of mice lung tissues with corresponding incidence of lung metastases. (*F*) Quantitative measurements of natural lipid peroxidation by-products *Left:* 4-HNE and *Right:* MDA in MHCC97L-NTC and MHCC97L-shFSP1 cells further suggest increased lipid peroxidation upon FSP1 knockdown. (*G*) Quantification of relative LDH release in MHCC97L-NTC and MHCC97L-shFSP1 cells demonstrated that intracellular lipid peroxidation induced by FSP1 knockdown significantly increased cell death. (*H*) SYTOX Green (SG^+) staining in MHCC97L-NTC and MHCC97L-shFSP1 cells demonstrated increased cell death from FSP1 knockdown were rescued with Fer-1. (*I*) Cell proliferation rates of MHCC97L-NTC and MHCC97L-shFSP1 cells determined using BrdU assay indicated that Fer-1, not inhibitors of other modes of RCD GSK'872 (necroptosis), Z-VAD-FMK (apoptosis), and MRT68921 (autophagy), can rescue proliferation rates suppressed by FSP1 knockdown. Error bars indicate mean ± SD. $^*P < .05$, $^{**}P < .01$, $^{***}P < .001$, $^{****}P < .0001$ vs NTC or Fer-1 as indicated. Student *t* test. *E*: scale bar = 1 cm

We further examined the effects of ferroptosis induction in human HCC using erastin (Selleck Chemicals, Houston, TX), another well-established ferroptosis inducer targeting the xCT antiporter and inhibiting the cysteine/GPX4 pathway.[31] We found that erastin significantly induced ferroptosis, suppressed HCC cell proliferation, and promoted

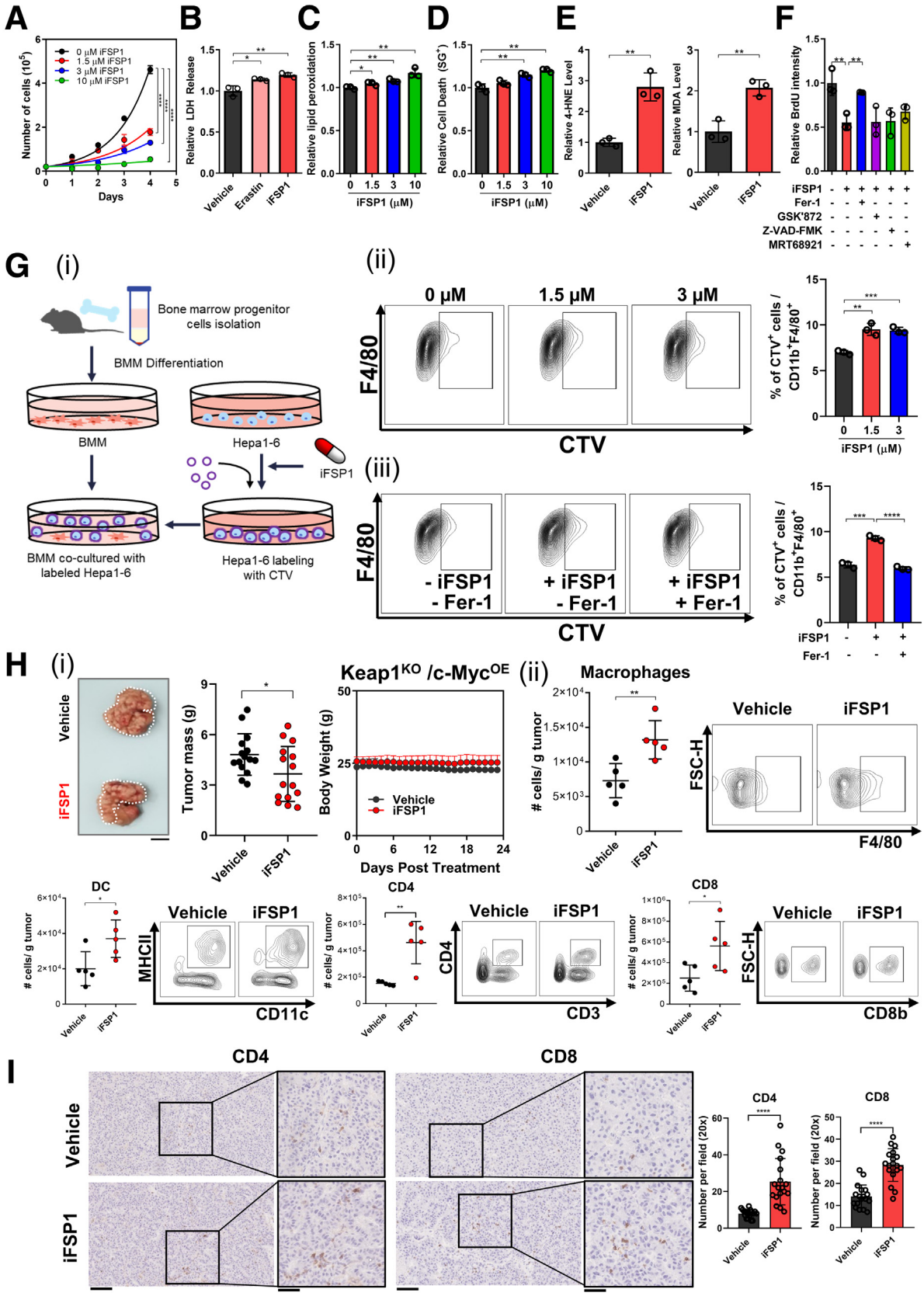

their uptake by BMMs in vitro (Figure 8*A*–*D*). Furthermore, erastin effectively inhibited HCC tumor growth in vivo, but in stark contrast to iFSP1, the number of intratumoral $CD4^+$ and $CD8^+$ T cells was also reduced (Figure 8*E*). The discrepancy in T cell number upon iFSP1 (FSP1 inhibitor) and erastin (GPX4 inhibitor) treatments in HCC tumors may be due to T cells' reliance on the GPX4 pathway to counteract ferroptosis.[17,32] Our findings illustrated that ferroptosis induction via FSP1 inhibition using iFSP1 suppressed HCC tumor growth not only through mediating HCC cell death, but also by altering the immune landscape of HCC tumors. Our findings highlight FSP1 inhibition as a unique anti-tumor strategy in comparison to other ferroptosis inducers.

Single-cell RNA Sequencing Revealed Immune Landscape Alteration Upon iFSP1 Treatment

To further explore immune landscape changes in HCC tumors upon iFSP1 treatment, we performed single-cell RNA sequencing (scRNA-seq) on single cells isolated from murine HDTVi-induced HCC tumors treated with iFSP1 or vehicle control (Figure 9*A*). Using unsupervised clustering analysis, we identified major immune cell populations by their marker genes. The representative marker genes were visualized by t-distributed stochastic neighbor embedding (tSNE) plots. These cell populations included B cells (*Cd19*), DCs (*Flt3*), macrophages (*Cd68*), monocytes (*Lyz2*), neutrophils (*Csf3r*), NK cells (*Ncr1*), pDCs (*Siglech*), T cells (Cd3e), and mast cells (*Cpa3*) (Figure 10*A*–*B*). Consistent with our observations from flow cytometry analysis, iFSP1 treatment resulted in increase of DCs, macrophages and T cells (Figure 10*C*).

We first investigated the myeloid compartment. Unsupervised clustering analysis further identified 4 DC subsets, 2 macrophage subsets, and 3 monocyte subsets (Figures 10*D*, 9*B*, 9*C*). All DC subsets increased upon iFSP1 treatment (Figure 10*E*). pDC represented plasmacytoid DCs expressing *Siglech, Irf8,* and *Bst2.* cDC1 expressed *Xcr1, Clec9a,* and *Batf3,* whereas cDC2 expressed *Cd209a, Itgax,* and *Clec10a,* corresponding to typical marker genes of conventional DC1 and conventional DC2, respectively (Figure 9*B*). cDC3 expressed *Fscn1, Ccl22,* and *Ccr7* (Figure 9*B*). It resembled a mature DC subset that expressed high level of activation and regulatory markers and shown to be derived from both cDC1 and cDC2.[33] This DC subset was also reported in multiple human cancer types as $LAMP3^+$ cDCs.[34] The 3 cDC subsets expressed a high level of major histocompatibility complex II molecules for antigen presentation (Figure 10*F*). For the 2 macrophage subsets, iFSP1 reduced Mac-1 and increased Mac-2 (Figure 10*E*). We further studied the differentially expressed genes among these 2 macrophage subsets. Interestingly, we found that Mac-2 was enriched in phagocytosis-related genes, such as *C1qa, C1qb, C1qc,* and *Mertk* (Figure 10*G*). Mac-2 also expressed a panel of receptors mediating phagocytosis (Figure 10*H*). These results illustrated that iFSP1 treatment recruit DCs with antigen presentation ability and phagocytic macrophages to tumor site.

We next studied subsets in T cells. We identified 2 $CD4^+$ and 4 $CD8^+$ T cell clusters, and they were annotated based on their marker gene expression (Figures 11*A*, 9*D*). Proliferating and exhausted $CD8^+$ T cells were particularly increased upon iFSP1 treatment (Figure 11*B*). Proliferating $CD8^+$ T cells are characterized by their expression of *Mki67*. Exhausted T cells expressed exhaustion markers including *Tox, Pdcd1, Lag3, Tigit,* and *Havcr2* (Figures 11*C*, 9*D*). Importantly, both T cell populations expressed multiple cytotoxic markers, including *Nkg7, Gzmk, Gzmb, Gzma,* and *Prf1* (Figure 11*D*). This suggested that iFSP1 treatment promoted tumor infiltration of $CD8^+$ T cells with cytotoxic functions.

To understand how these immune cells were recruited to tumor site, we then explored the expression of

Figure 5. (*See previous page*). iFSP1 induced ferroptosis and enhanced anti-tumor immune response. (*A*) Cell proliferation rates of MHCC97L cells determined by cell counting daily were significantly suppressed by treatments of 1.5, 3, and 10 μM FSP1 inhibitor iFSP1 in dose-dependent manner. (*B*) Quantification of relative LDH release from MHCC97L cells demonstrated that erastin and iFSP1 significantly induced cell death. (*C*) BODIPY 581/591 C_{11} staining in MHCC97L cells revealed significant increase of lipid peroxidation from treatments of 1.5, 3, and 10 μM iFSP1 in dose-dependent manner. (*D*) SYTOX Green (SG^+) staining in MHCC97L cells revealed that treatments of 1.5, 3, and 10 μM iFSP1 resulted in significant increase in cell death dose-dependently. (*E*) Quantitative measurements of *Left:* 4-HNE and *Right:* MDA in MHCC97L cells with iFSP1 or vehicle treatment further suggested iFSP1 significantly increased lipid peroxidation. (*F*) Cell proliferation rates of MHCC97L cells treated with iFSP1 and vehicle determined using BrdU assay indicated that Fer-1, not inhibitors of other modes of RCD GSK'872 (necroptosis), Z-VAD-FMK (apoptosis), and MRT68921 (autophagy), can rescue proliferation rates suppressed by iFSP1 treatment. (*G*) Extent of phagocytosis by BMMs of iFSP1 pre-treated Hepa1-6 cells was determined by phagocytosis assay. (*i*) Schematic representation of the experimental design. (*ii*) Ferroptotic Hepa1-6 cells induced by iFSP1 pre-treatment were more frequently phagocytosed by BMMs. (*iii*) Fer-1 treatment abrogated the increase of phagocytosis by BMMs of iFSP1 pre-treated Hepa1-6 cells. (*H*) In vivo HCC tumors were induced via HDTVi of plasmids carrying $Keap1^{KO}$/c-Myc^{OE} in C57BL/6N mice fed with HFD. (*I*) Administration of iFSP1 through intraperitoneal injection significantly reduced HCC tumor size compared with vehicle (n = 15 mice per experimental group). *Left:* Representative picture of harvested tumors. *Middle & Right:* Quantifications of tumor mass and body weight of mice. (*ii*) Administration of iFSP1 enhanced infiltration of macrophages, DCs, $CD4^+$ T cells, and $CD8^+$ T cells in HDTVi-induced HCC tumors. (*I*) IHC staining demonstrated the administration of iFSP1 enhanced the recruitment of $CD4^+$ and $CD8^+$ T cells in HDTVi-induced HCC tumors. *Left:* Representative staining of $CD4^+$ and $CD8^+$ T cells from harvested tumors treated with Vehicle or iFSP1. *Right:* Quantifications of number of $CD4^+$ and $CD8^+$ T cells stained per field. Error bars indicate mean ± SD. $^*P < .05$, $^{**}P < .01$, $^{***}P < .001$, $^{****}P < .0001$ vs vehicle or 0 μM as indicated. Student's *t* test. *H*: Scale bar = 1 cm. *I*: original = 20× magnification, scale bar = 100 μm; Inset = 40× magnification, scale bar = 50 μm

chemokines and observed that *Cxcl9* and *Cx3cl1* were induced in multiple DC and macrophage populations upon iFSP1 treatment (Figure 11*E*). CXCL9 is a well-known chemoattractant for CXCR3^{+} T cells, whereas CX3CL1 recruit DCs and macrophages expressing receptor CX3CR1. Moreover, we observed induction of costimulatory receptor, *Cd40* expression on DCs and macrophages and *Pdcd1*, encoding PD-1, on T cells (Figure 11*F*), pointing to potential targets for combination treatment.

As a systemic treatment, it is possible that iFSP1 also influences immune cell populations; therefore, we studied the expression of anti-ferroptotic genes in major immune cell populations. Interestingly, we found that immune cells expressed a high level of *Gpx4* but a low level of *Fsp1* (Figure 11*G*). Moreover, components of xCT antiporter were generally expressed in major immune cell populations (Figure 9*E*), suggesting that immune cells greatly rely on the GPX4 pathway to protect themselves from ferroptosis. This could also explain the reduction in T cells we observed in erastin-treated tumors.

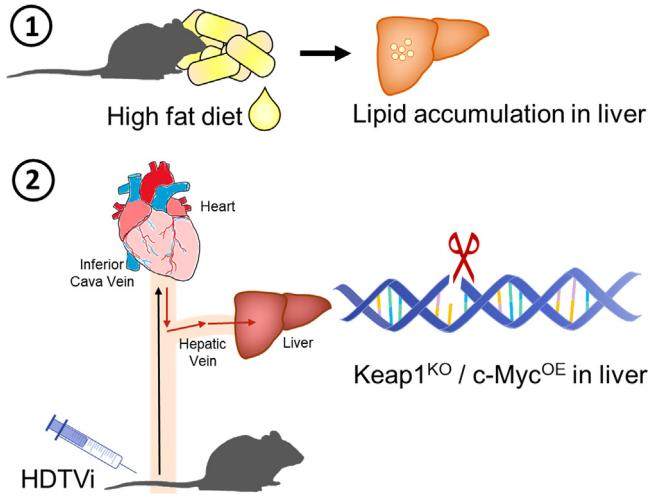

Figure 6. Schematic diagram illustrating murine HCC model used for iFSP1 efficacy testing. *In vivo* HCC tumors were induced in HFD-fed C57BL/6N mice by HDTVi of plasmids carrying Keap^{KO}/c-Myc^{OE}.

iFSP1 in Combination With Immunotherapies Effectively Prolonged HCC Survival

The upregulation of PD-1 on T cells and CD40 expression on DCs and macrophages prompted us to explore the synergistic effect of iFSP1 and immunotherapies. HCC tumors were induced by HDTVi in mice fed with HFD, and mice were treated with iFSP1 in combination with either ICIs (anti-PD-1 and anti-PD-L1; BioXcell, Lebanon, NH), or a new generation of immunotherapy, CD40 agonist (BioXcell). Single treatment of iFSP1 or anti-PD-1 improved survival of tumor-bearing mice similarly, whereas co-administration of them effectively prolonged survival of mice (Figure 12*A*). Interestingly, iFSP1 showed better efficacy in prolonging survival than anti-PD-L1 as a single treatment in our HCC model. Combining iFSP1 and anti-PD-L1 can further extend the survival of HCC-bearing mice (Figure 12*B*). Apart from the 2 ICIs currently used in patients with HCC, we also explored the effect of CD40 agonist in combination with iFSP1. CD40 agonist worked with iFSP1 to prolong the survival of tumor-bearing mice (Figure 12*C*). Here, we demonstrated that iFSP1 treatment can improve or potentiate the effect of multiple immunotherapies without adverse effects on body weight (Figure 13). Our results suggested that iFSP1 treatment recruited APCs and promoted antigen presentation by APCs to T cells. This is further enhanced by immunotherapies that either reinvigorate T cells (anti-PD-1 and anti-PD-L1) or activate APCs (CD40 agonist) (Figure 12*D*).

Discussion

Ferroptosis, as a distinct form of cell death, was first reported to suppress cancer in 2003; however, the implications of ferroptosis in cancers were only revealed in recent years.[35] A CRISPR-Cas9 screening identified that peroxisome genes drove GPX4 inhibitor-induced ferroptosis in ovarian cancer cells by promoting polyunsaturated ether phospholipid synthesis.[36] Another study revealed that therapy-resistant lung and pancreatic cancer cells were highly dependent on GPX4 and thus particularly susceptible to ferroptosis inducers.[37] A recent study demonstrated that ferroptosis inhibits metastasis. Melanoma cells in the blood were shown to encounter a higher level of ferroptosis than melanoma cells in the lymph, resulting in more melanoma metastases formed from lymph node metastasis than vascular metastasis.[38] Interestingly, triple-negative breast cancer cells express higher levels of pro-ferroptotic genes (TfR and ACSL4) and lower levels of anti-ferroptotic genes (ferritin heavy chain 1, ferroportin, GPX4, GSH synthetase) and are therefore more susceptible to ferroptosis.[39] The roles of ferroptosis in HCC, especially FSP1-driven mechanisms, have not been fully explored. Our study unprecedentedly reported that HCC is reliant on FSP1 for protection against ferroptosis rather than GPX4, as we showed that FSP1 is upregulated in human HCC but not GPX4. FSP1 deficiency led to decreased ubiquinol-to-ubiquinone ratio, diminishing the ability of cancer cells to counteract lipid peroxidation. This induced ferroptosis in cancer cells and suppressed HCC tumor progression.

Multiple pathways are involved in the regulation of ferroptosis. P53 transcriptionally represses SLC7A11 to inhibit cysteine intake, which leads to ROS-induced ferroptosis in osteosarcoma, NSCLC, and breast cancer cells.[40] Meanwhile, NRF2, the master regulator of antioxidant response, has been shown to protect HCC cells from ferroptosis.[41,42] In HCC cells treated with ferroptosis inducers such as erastin and sorafenib, P62 releases NRF2 from KEAP1 binding, thereby stabilizing NRF2 so that NRF2 mediates the transcription of NQO1, heme oxygenase-1, and FTH1 to counteract ferroptosis.[42] NRF2 inhibitor worked synergistically with these ferroptosis inducers to inhibit HCC growth in mice by eliciting severe ferroptosis in HCC cells.[42] In this study, we showed for the first time that FSP1 is transcriptionally regulated by NRF2. NRF2 inhibitors such as

clobetasol propionate, which we previously showed to have remarkable anti-tumor effects in HCC, are likely to induce ferroptosis through inhibiting GPX4 and FSP1 pathways.[27] However, systemic administration of NRF2 inhibitors might also elicit ferroptosis of immune cells, affecting the combined effects with ICIs and CD40 agonist.

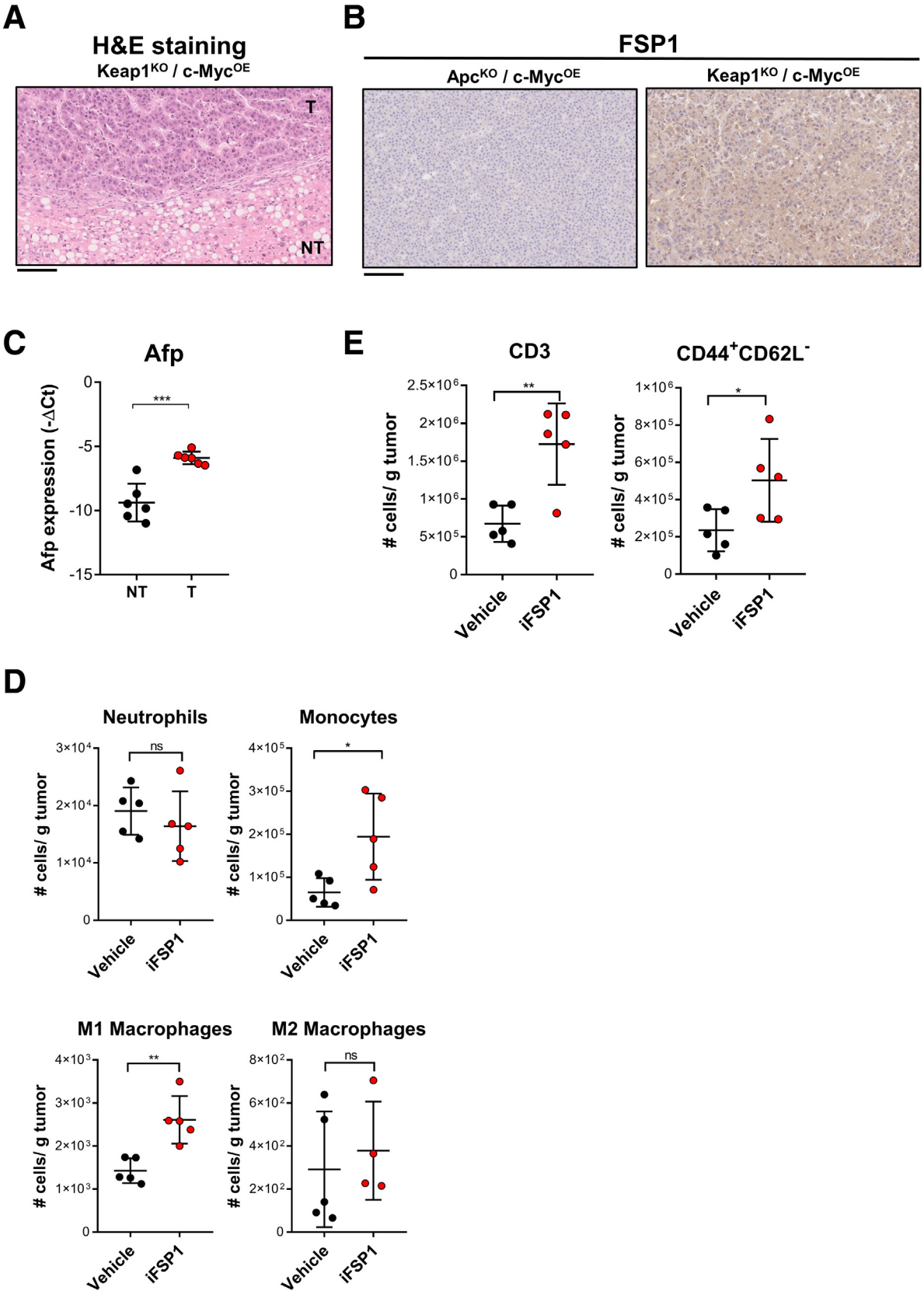

Ferroptosis is a form of ICD. Multiple studies illustrated that ferroptotic cancer cells released DAMPs such as ATP, HMGB1, and oxidized phospholipids, which promoted their uptake by DCs and macrophages.[43,44] However, whether and how ferroptosis induction in cancer promotes anti-tumor immune responses are yet to be investigated. Here, we showed that induction of ferroptosis by FSP1 inhibition suppressed HCC tumor growth. This anti-tumor effect is not only due to the direct induction of cell death but also the activation of anti-tumor immune responses. We demonstrated that iFSP1 treatment suppressed HCC progression and promoted infiltration of antigen presenting DCs, phagocytic macrophages, and cytotoxic T cells into tumor. These immune cells could be recruited by chemokines that were upregulated upon iFSP1 treatment. CXCL9 is a well-studied chemokine that is important for $CXCR3^+$ T cell trafficking and recruitment to tumor site.[45,46] CX3CL1 could also mediate the recruitment of DCs and macrophages expressing CX3CR1.[47,48] A recent study reported that ICIs (anti-CTLA4 and anti-PD-L1) could induce ferroptosis of cancer cells by unleashing the IFN-γ-producing capability of $CD8^+$ T cells.[49] IFN-γ produced by activated $CD8^+$ T cells suppresses the protein expression of components in the xCT antiporter (SLC7A11 and SLC3A2), thereby inducing ferroptosis.[49] This study mainly focuses on how T cells induce ferroptosis of cancer cells, whereas our study revealed that induction of ferroptosis in cancer cells could reciprocally promote T cell tumor infiltration. Together, these suggest a potential feedforward loop to suppress cancer progression.

Drugs that induce ICD are being hotly pursued because of their potential as combination treatments with ICIs in multiple cancer types.[50] Suboptimal responses to ICIs could be due to the insufficient antigen presentation.[51] Treatments inducing ICD lead to the release of tumor antigens and DAMPs by cancer cells and thus recruiting APCs to engulf the tumor antigens. This enhances antigen presentation by APCs to T cells, initiating anti-tumor immune response.[52] Upon iFSP1 treatment, we observed an upregulation of CD40 on DCs and macrophages while PD-1 on T cells. Excitingly, we showed that combination treatment of iFSP1 and anti-PD-1, anti-PD-L1, or CD40 agonist can all prolong survival of tumor-bearing mice. Although anti-PD-1 and anti-PD-L1 aim at blocking PD-1 and PD-L1 ligation and thus reinvigorating T cells, CD40 agonist enhances antigen presentation ability of APCs and promotes the secretion of a plethora of pro-inflammatory cytokines and has been demonstrated to effectively suppress cholangiocarcinoma.[53-55] CD40 agonist demonstrated clinical activity when used in combination with chemotherapies and nivolumab in treating metastatic pancreatic adenocarcinoma, whereas its effects in HCC remain to be investigated.[56] Recently, it was reported that TYRO3 is also an anti-ferroptotic gene through inducing NRF2-mediated transcription to suppress lipid ROS accumulation. Cancers with TYRO3 overexpressed are resistant to anti-PD-1 treatment, indirectly suggesting that ferroptosis improves the efficiency of ICIs.[57] Together with our findings, these show that ferroptosis induction could work synergistically with immunotherapies and shed light on a novel therapeutic approach for HCC.

The effects of ferroptosis inducers on immune cells require closer investigation. Interestingly, our flow cytometry data showed that total CD4 T cells were enriched in HCC from iFSP1-treated mice, whereas scRNA-seq data showed that the percentage of CD4 central memory T cells decreased. Although the detailed mechanisms explaining why CD4 central memory T cells are reduced remain unknown, studies showed that anti-PD-1/PD-L1 treatment was expected to promote the memory of T cells, further providing mechanistic explanation to combine iFSP1 with ICIs.[58] A recent study showed that CD36 on $CD8^+$ T cells increased their fatty acids uptake and lipid peroxidation.[59] This contributed to $CD8^+$ T cell ferroptosis and suppressed its cytotoxic functions, whereas CD36 blockade could enhance anti-tumor response.[59] Most recently, it was further shown that the CD36-mediated $CD8^+$ T cell dysfunction could be rescued by GPX4 overexpression.[17] Another study performed a high throughput pharmacologic screening to identify specify metabolic vulnerabilities of $CD8^+$ T cells and cancer cells and showed that $CD8^+$ T cells are more susceptible to RSL3, a GPX4 inhibitor, than cancer cells.[32] These indicated T cells highly rely on GPX4 pathway as a protective mechanism against ferroptosis. Our data showed that the dose of iFSP1 we used for in vivo treatment did not influence the T cell population, but we did observe a reduction in T cell population in GPX4 inhibitor (erastin)-treated tumors despite the suppression of tumor growth. This discrepancy could be due to the reliance of immune cells on the GPX4 pathway to protect themselves from ferroptosis because our scRNA-seq analysis demonstrated that immune cells in general only express GPX4 but not FSP1. Despite the tumor-suppressing effect of inhibitors targeting GPX4 pathway, immune cells also rely on GPX4 pathway to protect them from ferroptosis. Therefore, GPX4 inhibition may not fully demonstrate the potential of ferroptosis inducers as cancer treatment because it could

Figure 7. (***See previous page***). **Characterization of murine tumor model used and the immune landscape change upon iFSP1 treatment.** (*A*–*C*) In vivo HCC tumors were induced via HDTVi of plasmids carrying $Keap1^{KO}$/$c\text{-}Myc^{OE}$ (or Apc^{KO}/$c\text{-}Myc^{OE}$) in C57BL/6N mice fed with HFD. (*A*) Representative hematoxylin and eosin staining of $Keap1^{KO}$/$c\text{-}Myc^{OE}$ HCC tumor. (*B*) Representative staining of FSP1 expression from Apc^{KO}/$c\text{-}Myc^{OE}$ or $Keap1^{KO}$/$c\text{-}Myc^{OE}$ HCC tumors at protein level by IHC staining. (*C*) RT-qPCR demonstrated the upregulation of *Afp* in tumorous (T) tissues when compared with NT liver tissues in $Keap1^{KO}$/$c\text{-}Myc^{OE}$ HCC tumor. (*D*) Administration of iFSP1 altered myeloid cells infiltration, including neutrophils ($CD11b^+$ $Ly6G^+$), monocytes ($CD11b^+$ $Ly6C^+$), M1 macrophages ($CD11b^+$ $F4/80^+$ $CD86^+$ $MHCII^+$), and M2 macrophages ($CD11b^+$ $F4/80^+$ $CD206^+$) in HDTVi-induced HCC tumors. (*E*) Administration of iFSP1 increased number of T cells ($CD3^+$) and T effector cells ($CD44^+$ $CD62L^-$) in HDTVi-induced HCC tumors. $^*P < .05$, $^{**}P < .01$, $^{***}P < .001$ vs NT or vehicle as indicated. Student *t* test. *A*–*B*: 20× magnification, scale bar = 100 μm.

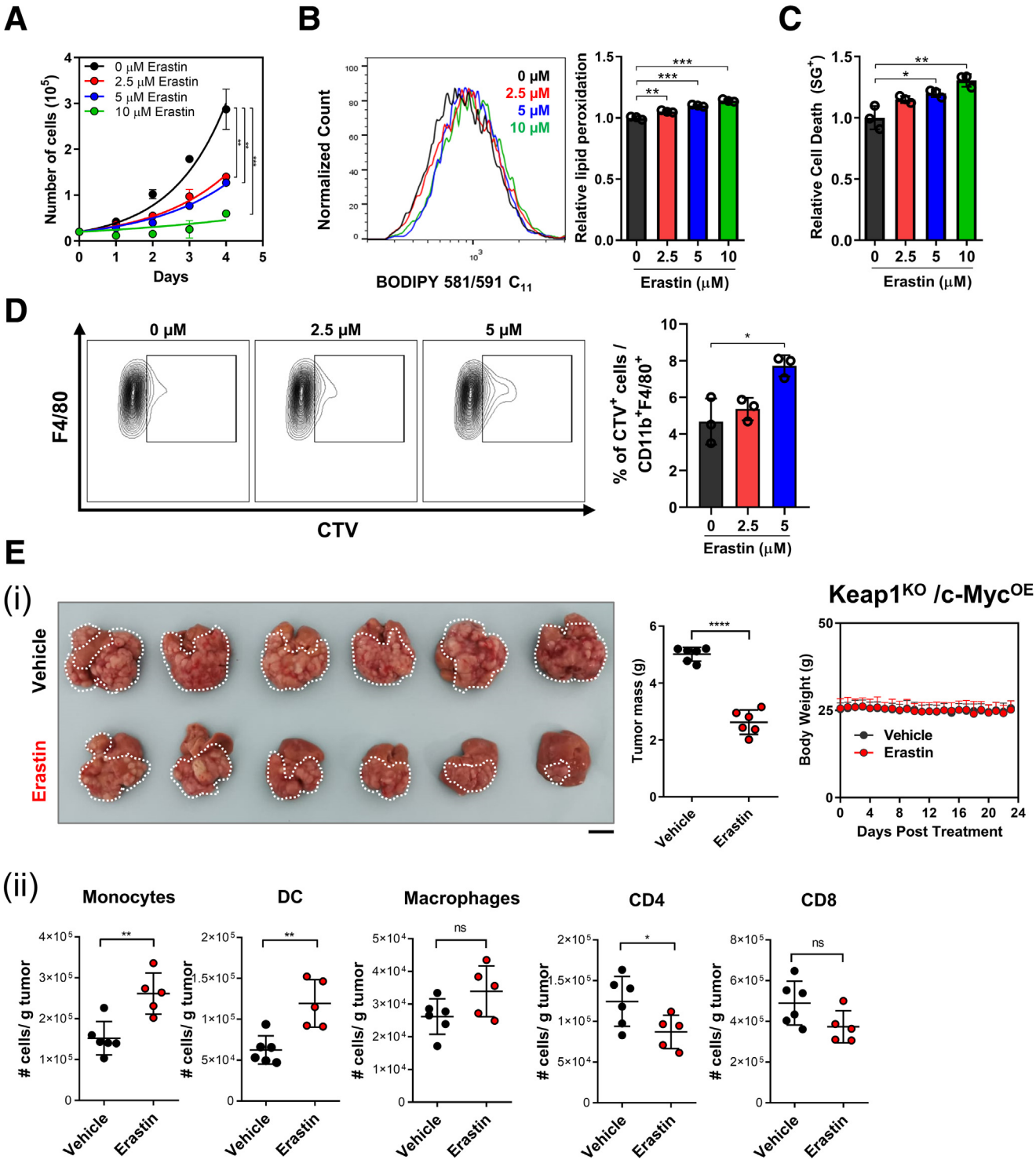

Figure 8. Erastin effectively induced ferroptotic HCC cell death. (*A*) Cell proliferation rates of MHCC97L cells determined by cell counting daily were significantly suppressed by treatments of 2.5, 5, and 10 μM ferroptosis inducer erastin in dose-dependent manner. (*B*) BODIPY 581/591 C_{11} staining in MHCC97L cells revealed significant increase of lipid peroxidation from treatments of 2.5, 5, and 10 μM erastin in dose-dependent manner. (*C*) SYTOX Green (SG^+) staining in MHCC97L cells revealed that treatments of 2.5, 5, and 10 μM erastin resulted in significant increase in cell death dose-dependently. (*D*) Ferroptotic Hepa1-6 cells induced by erastin pre-treatment were more frequently phagocytosed by BMDMs. (*E*) In vivo HCC tumors were induced via HDTVi of plasmids carrying $Keap1^{KO}$/c-Myc^{OE} in C57BL/6N mice fed with HFD. (*i*) Administration of erastin through intrperitoneal injection significantly reduced HCC tumor size compared with vehicle (n = 6 mice per experimental group). *Left:* Representative picture of harvested tumors. *Middle & Right*: Quantifications of tumor mass and body weight of mice. (*ii*) Administration of erastin increased the number of monocytes, DCs and macrophages, while it decreased the number of $CD4^+$ T cells and $CD8^+$ T cells in HDTVi-induced HCC tumors. Error bars indicate mean ± SD. $^*P < .05$, $^{**}P < .01$, $^{***}P < .001$, $^{****}P < .0001$ vs vehicle or 0 μM as indicated. Student *t* test. *E*: Scale bar = 1 cm.

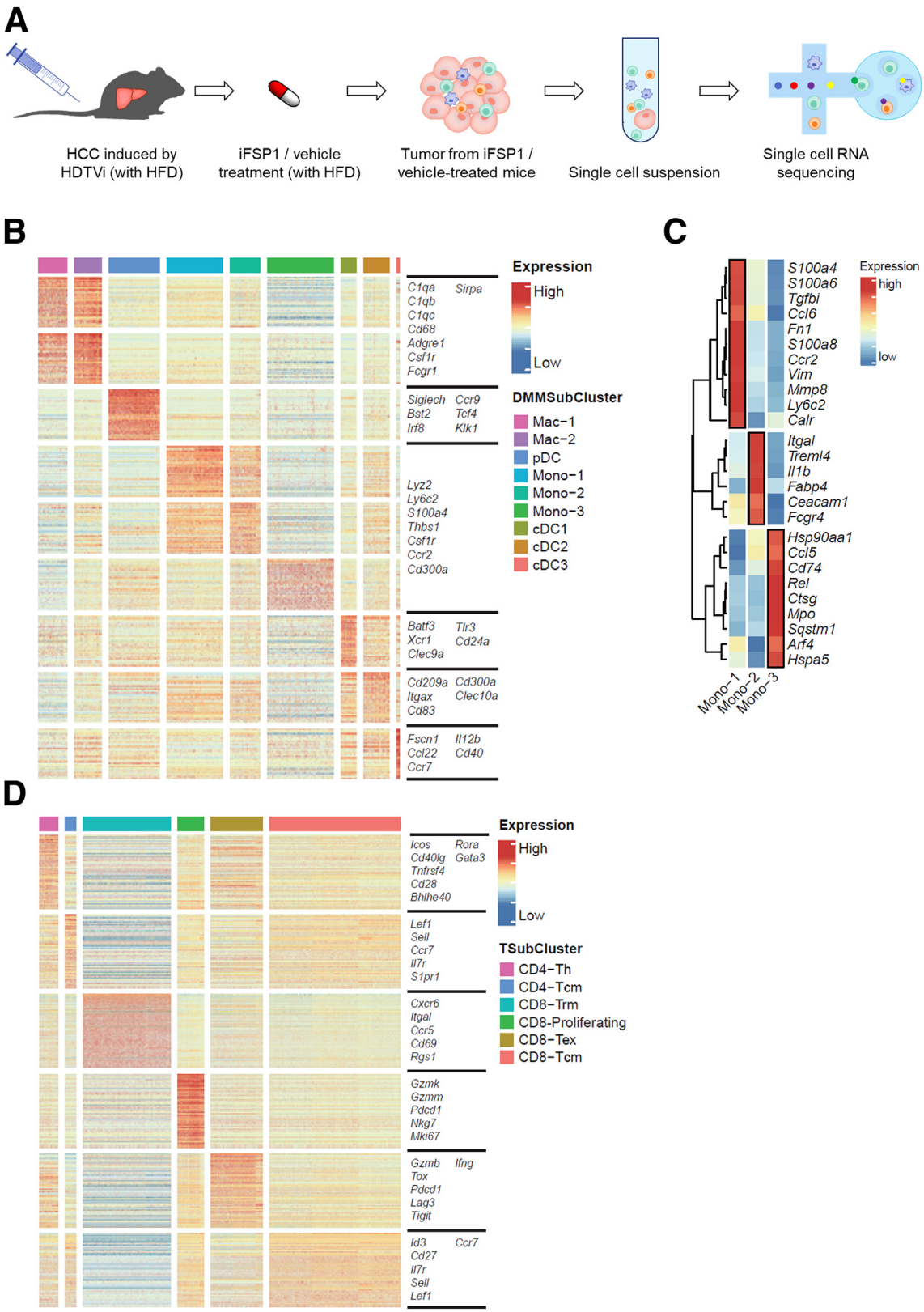

Figure 9. ScRNA-seq revealed iFSP1 altered immune landscape in mouse HCC. (*A*) Schematic diagram illustrating experimental design. (*B*) Gene expression heatmap of myeloid clusters showed the selected marker genes for each subset. (*C*) Gene expression heatmap of monocytes showed the selected marker genes for each subset. (*D*) Gene expression heatmap of T cells showed the selected marker genes for each subset. *B, D*: Expression: Z-score normalized expression. *C*: Expression: Z-score normalized mean expression.

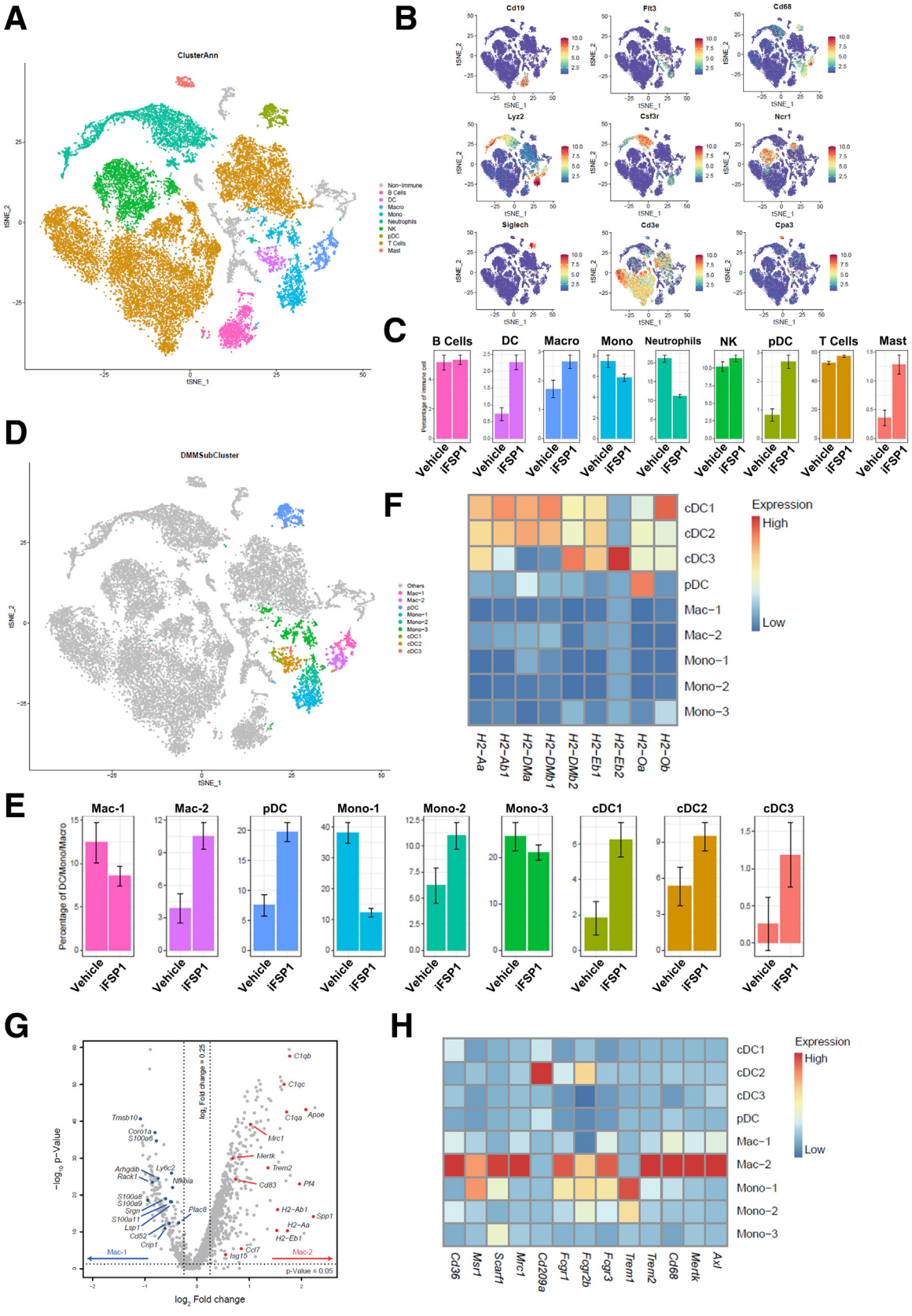
A
ClusterAnn
Non−Immune
B Cells
DC
Macro
Mono
Neutrophils
NK
pDC
T Cells
Mast
tSNE_1
tSNE_2
B
Cd19
Flt3
Cd68
Lyz2
Csf3r
Ncr1
Siglech
Cd3e
Cpa3
C
B Cells
DC
Macro
Mono
Neutrophils
NK
pDC
T Cells
Mast
Percentage of immune cell
Vehicle
iFSP1
D
DMMSubCluster
Others
Mac−1
Mac−2
pDC
Mono−1
Mono−2
Mono−3
cDC1
cDC2
cDC3
E
Mac-1
Mac-2
pDC
Mono-1
Mono-2
Mono-3
cDC1
cDC2
cDC3
Percentage of DC/Mono/Macro
F
cDC1
cDC2
cDC3
pDC
Mac−1
Mac−2
Mono−1
Mono−2
Mono−3
H2−Aa
H2−Ab1
H2−DMa
H2−DMb1
H2−DMb2
H2−Eb1
H2−Eb2
H2−Oa
H2−Ob
Expression
High
Low
G
−log10 p−Value
log2 Fold change
log2 Fold change = 0.25
p-Value = 0.05
Mac-1
Mac-2
C1qb
C1qc
C1qa
Apoe
Mrc1
Mertk
Trem2
Cd83
Pf4
H2−Ab1
Spp1
H2−Aa
H2−Eb1
Ccl7
Isg15
Tmsb10
Coro1a
S100a6
Arhgdib
Rack1
Ly6c2
Nfkbia
S100a8
S100a9
Srgn
S100a11
Lsp1
Cd52
Crip1
Plac8
H
cDC1
cDC2
cDC3
pDC
Mac−1
Mac−2
Mono−1
Mono−2
Mono−3
Cd36
Msr1
Scarf1
Mrc1
Cd209a
Fcgr1
Fcgr2b
Fcgr3
Trem1
Trem2
Cd68
Mertk
Axl
Expression
High
Low

dampen the immune responses. This highlights the importance of further investigation to identify a molecular target that can selectively induce ferroptosis in cancer cells but not immune cells. We showed that FSP1 is overexpressed in human HCC but not GPX4, whereas tumor-infiltrating immune cells express a high level of GPX4 but not FSP1. These suggest that cancer cells and immune cells rely on different mechanisms to protect themselves from ferroptosis in HCC. Therefore, FSP1 could be a superior candidate because its inhibition selectively induces ferroptosis in HCC cells and unleashes anti-tumor immune responses.

Materials and Methods

The Cancer Genome Atlas

Transcriptome sequencing results on 49 pairs of human HCC and corresponding NT liver tissues were retrieved from TCGA through cBioportal (http://www.cbioportal.org/). The mRNA expression levels of FSP1, TF, and GPX4 were examined. Correlation between expression levels of FSP1 and antioxidant genes TKT, ME1, MTHFD1L, NQO1, AKR1B10, and AKR1C1 in human HCC and NT liver tissues were also retrieved from TCGA.

Clinical Samples

Paired clinical HCC tumor and NT liver tissues were used in this study. Tissue samples were collected from patients with HCC admitted to Pamela Youde Nethersole Eastern Hospital, Queen Elizabeth Hospital, and/or Queen Mary Hospital. Resected tissue samples were snap-frozen with liquid nitrogen and stored at −80 °C for future use. Approval for the use of clinical HCC tumor samples and paired NT liver tissues was previously obtained from the Institutional Review Board of The University of Hong Kong and the Hospital Authority of Hong Kong (HKU/HA HKW IRB; ref. no. UW 09-158). Prior to the collection and use of resected clinical tissues, signed consents were obtained as acknowledgements from patients.

Immunohistochemical Staining

Clinical human and mouse HCC/NT tissues fixed in 4% formalin and 75% ethanol were embedded in paraffin. Before IHC staining, paraffin sections were dewaxed with xylene and rinsed with ethanol. Antigen retrieval was performed by boiling in EDTA buffer, and the liver tissue sections were stained with primary antibody (Table 2) at 4 °C overnight, followed by horseradish peroxidase-conjugated secondary antibody (Dako, Glostrup, Denmark) staining at room temperature for 30 minutes. Sections were developed using 3,3'-diaminobenzidine (Sigma-Aldrich) and counterstained with hematoxylin.

Chromatin Immunoprecipitation

HCC cells were fixed in 3.7% formaldehyde for DNA crosslinking followed by sonication. Antibodies against NRF2 and IgG control (Table 2) were added to sheared DNA fragments. DNA-protein-antibody complexes were incubated with Protein A/Salmon Sperm DNA Agarose Beads (Merck Millipore, Burlington, MA), sequentially washed using gradients of salt buffer, and eluted in 1% SDS/$NaHCO_3$. ChIP DNA samples were analyzed by RT-qPCR with primers flanking the putative ARE (Table 3).

Luciferase Reporter Assay

Oligonucleotides containing FSP1 WT or MUT AREs were inserted into the pGL4 firefly luciferase promoter reporter vector. Insert sequences were included in Table 4. These plasmids containing WT or MUT AREs were transfected into Huh7 cells (-NTC, -shNRF2 and -shMAF) together with pRL-CMV and treated with 10μM tBHP for 24 hours. Luciferase activities were determined using the Dual-Luciferase Reporter System (Promega) according to the manufacturer's instructions.

Establishment of Stable Cell Lines

As previously described, stable-knockdown HCC cell lines were established using lentiviral-mediated approach.[60-62] Briefly, shRNAs targeting NRF2 (shNRF2), KEAP1 (shKEAP1), FSP1 (shFSP1), MAF (shMAF), or NTC contained within pLKO.1-puro vectors were stably transfected into HCC cells. Puromycin was used to select HCC cells that stably express the shRNA-containing vectors. Sequences of all shRNAs used are provided in Table 4.

HCC Cell Culture

Multiple human HCC cell lines including MHCC97L, PLC/PRF/5, Huh7, and a mouse HCC cell line (Hepa 1-6) were used in this study. MHCC97L and Huh7 were kind gifts from Dr Z.Y. Yang of Fudan University (Shanghai, China) and Professor H. Nakabayashi of Hokkaido University School of Medicine (Sapporo, Japan), respectively. PLC/PRF/5 and

Figure 10. (***See previous page***). **iFSP1 promoted anti-tumorigenic immune cells infiltration.** (*A*) tSNE plot revealed clusters of major cell populations isolated from mouse HCC tumor treated with iFSP1 or vehicle. (*B*) tSNE plots showed the selected marker genes of major immune cell populations. (*C*) Percentage change of major immune cell clusters revealed the increase of DCs, macrophages, and T cells in tumor upon iFSP1 treatment. (*D*) tSNE plot illustrated further sub-clustering of selected myeloid cells. (*E*) Percentage change of myeloid cell subsets demonstrated iFSP1 treatment led to an increase in all DC subsets but differential effect on macrophages and monocytes. (*F*) Heatmap showing expression of major histocompatibility complex II genes in the myeloid subsets indicated that DCs expressed the highest level of antigen-presenting signature. (*G*) Volcano plot showing differentially expressed genes between Mac-1 and Mac-2 revealed that phagocytosis-related genes were enriched in Mac-2. *P*-value $< .05$ and $\log_2$ (fold change) > 0.25. (*H*) Heatmap showing expression of phagocytosis-related genes in the myeloid subsets indicated that Mac-2 expressed the highest level of phagocytic signature. *B*: Expression: normalized expression. *C, E*: Error bars indicate 95% confidence interval. *F, H*: Expression: Z-score normalized mean expression.

Hepa 1-6 were obtained from American Type Culture Collect (Manassas, VA). All cell lines were cultured in Dulbecco's Modified Eagle Medium-high glucose media with 10% fetal bovine serum (FBS) and 1% penicillin-streptomycin (P/S) supplementations (all reagents from Gibco by Life Technologies, Grand Island, NY). Cells were cultured in a 37 °C

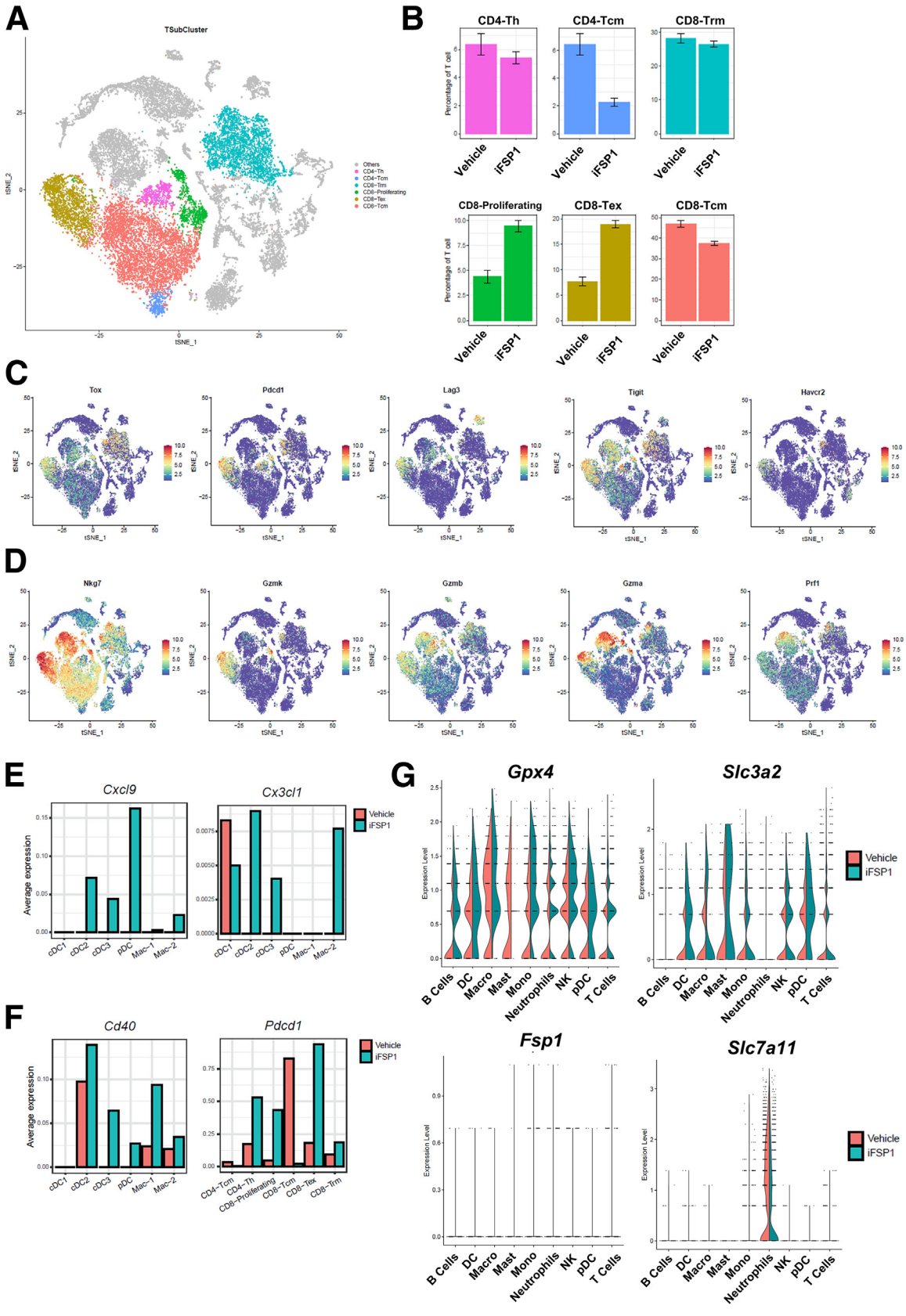

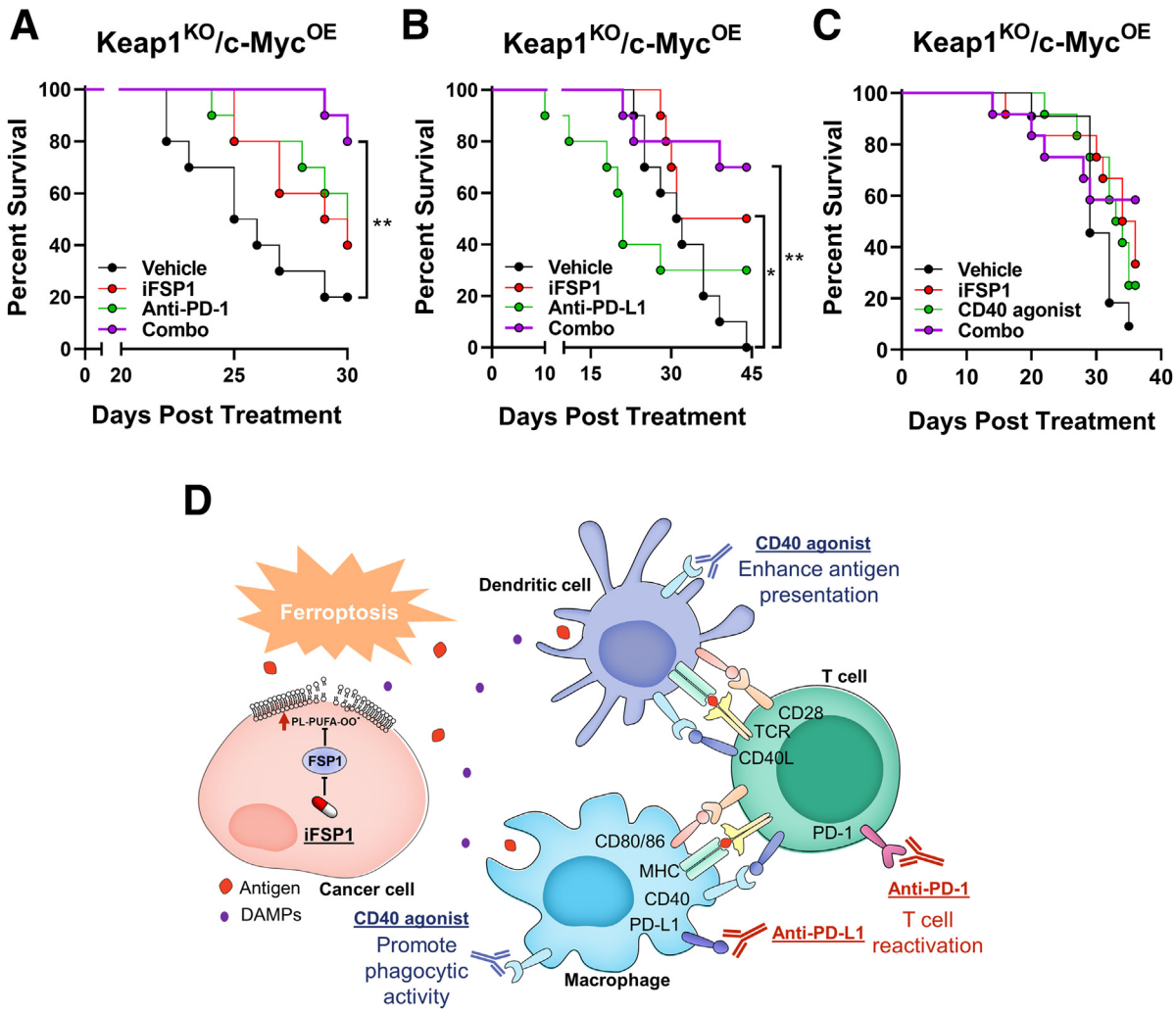

Figure 12. Combination of iFSP1 and immunotherapies prolonged HCC survival. (*A–B*) Co-administrations of iFSP1 with ICIs, *(A)* anti-PD-1 and *(B)* anti-PD-L1 antibodies, respectively, synergistically prolonged the survival of tumor-bearing C57BL/6N mice (n = 10 mice per experimental group). (*C*) Co-administrations of iFSP1 and CD40 agonist prolonged the survival of tumor-bearing C57BL/6N mice (n = 12 mice per experimental group). (*D*) Schematic summary of immunomodulatory effects and treatment strategies of iFSP1. *A–C*: Log-rank test.

humidified incubator supplied with 5% CO_2. Authentication of all cell lines within this study was performed using the AuthentiFiler PCR Amplification Kit (Applied Biosystems, Foster City, CA). All authenticated cell stocks were thawed and used within 4 passages.

RNA Extraction, Reverse Transcription, and RT-qPCR

Total RNA was extracted from paired clinical HCC/NT liver tissues, which were snap-frozen with liquid nitrogen and stored at −80 °C, and HCC cell lines with TRIzol reagent (Ambion by Life Technologies, Austin, TX). Purified RNA samples were synthesized into cDNA by reverse transcription using GeneAmp RNA PCR Core Kit (Applied Biosystems). From paired clinical HCC/NT liver tissue samples, RT-qPCR amplifications of FSP1 and internal control 18S were performed using TaqMan Gene Expression Assay (Applied Biosystems). RT-qPCR amplifications of NRF2, KEAP1, FSP1, internal control 18S from HCC cell lines, and Afp and Gapdh from mouse HCC/NT liver tissue samples were performed using SYBR Green PCR Master

Figure 11. (***See previous page***). **ScRNA-seq revealed FSP1 as a potent therapeutic target in HCC.** (*A*) tSNE plot showed further clustering of T cells into 6 subsets. (*B*) Percentage change of T cell subsets revealed an increase in proliferating and exhausted $CD8^+$ T cells upon iFSP1 treatment. (*C*) tSNE plots showed the expression level of T cell exhaustion markers. (*D*) tSNE plots showed the expression level of cytotoxic markers. (*E*) Average expression level of *Cxcl9* and *Cx3cl1* were induced upon iFSP1 treatment in DC and macrophage subsets. (*F*) Average expression level of *Cd40* in DC and macrophage subsets and *Pdcd1* in T cell subsets were induced upon iFSP1 treatment. (*G*) Left: Violin plots showed the expression level of *Gpx4* and *Fsp1*in major immune cell populations. Right: Violin plots showed the expression level of Slc3a2 and Slc7a11 in major immune cell populations. *B*: Error bars indicate 95% confidence interval. *C–G*: Expression: normalized expression.

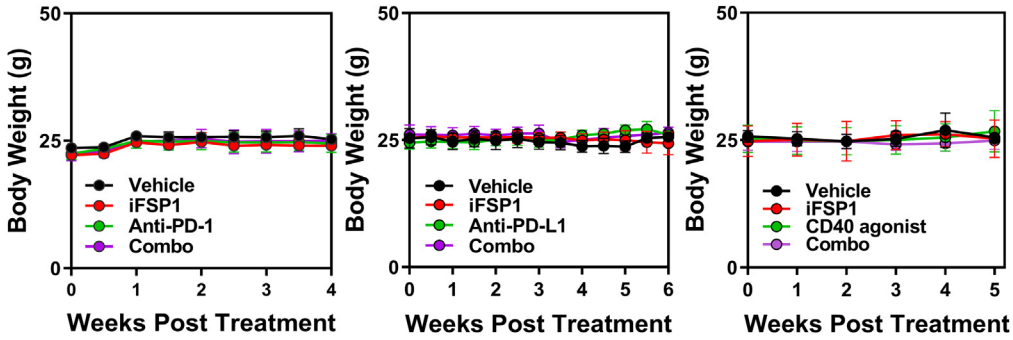

Figure 13. Body weights of mice upon drug administration. Body weights of tumor-bearing mice co-treated with iFSP1 and anti-PD-1, anti-PD-L1, or CD40 agonist.

Mix (Applied Biosystems) with the respective RT-qPCR primers listed in Table 3. All RT-qPCR amplifications were performed using the StepOne Real-Time PCR System (Applied Biosystems).

Protein Extraction and Western Blotting

Total protein lysates from human HCC cell lines were extracted using RIPA lysis buffer with cOmplete protease and PhosSTOP phosphatase inhibitor supplementations (both from Roche Diagnostics, Mannheim, Germany). Equal volumes of protein lysates were separated by SDS-PAGE and transferred onto PVDF membranes (GE Healthcare, Little Chalfont, UK). Protein expression of targeted genes were determined with their respective antibodies listed in Table 2.

Liquid Chromatography-mass Spectrometry

Ubiquinol/ubiquinone were extracted from HCC cells plated on 10-cm culture dishes at 70% to 80% confluence using cold pure methanol. Supernatants from all pelleted samples were transferred to new tubes, dried using a vacuum concentrator, and reconstituted with 100 μL methanol. LC-MS analyses were performed on a ExionLC AC System coupled with X500R QTOF (Sciex Applied Biosystems, Framingham, MA) mass spectrometer. Samples were separated with isocratic elution of methanol containing 2 mM ammonium acetate at a flow rate of 0.4 mL/minute using an ACQUITY UPLC BEH C18 reverse-phase column (2.1 mm $\times$ 50 mm, 1.7 μm).[63] The column temperature was kept at 40 °C. The mass spectrometer was operated in positive ionization mode. Quantification of $CoQ_{10}H_2$ and CoQ_{10} were performed using TOF-MS/MS as $[M + NH_4]^+$ with the

Table 2. Antibodies Used

Antibody	Source	Application	Clone	Cat no.	Company
NRF2	Rabbit	ChIP	/	ab62352	Abcam
IgG control	Rabbit	ChIP	/	sc-2027	Santa Cruz
CD16/32	Mouse	Flow cytometry	93	101301	Biolegend
CD45	Mouse	Flow cytometry	30-F11	103127	Biolegend
CD8b	Mouse	Flow cytometry	YTS156.7.7	126619	Biolegend
CD44	Mouse	Flow cytometry	IM7	103005	Biolegend
CD62L	Mouse	Flow cytometry	MEL-14	104431	Biolegend
CD45	Mouse	Flow cytometry	30-F11	103115	Biolegend
CD3	Mouse	Flow cytometry	17A2	100205	Biolegend
CD4	Mouse	Flow cytometry	GK1.5	100429	Biolegend
CD11b	Mouse	Flow cytometry	M1/70	101205	Biolegend
Ly6C	Mouse	Flow cytometry	HK1.4	128017	Biolegend
Ly6G	Mouse	Flow cytometry	1A8	127623	Biolegend
CD11c	Mouse	Flow cytometry	N418	117307	Biolegend
F4/80	Mouse	Flow cytometry	BM8	123115	Biolegend
I-A/I-E	Mouse	Flow cytometry	M5/114.15.2	107625	Biolegend
CD8a	Mouse	IHC	D4W2Z	98941	Cell Signaling
CD4	Mouse	IHC	D7D2Z	25229	Cell Signaling
FSP1	Rabbit	IHC	/	20886-1-AP	Proteintech
FSP1	Rabbit	Western blot	/	PA5-28727	Invitrogen
β-actin	Mouse	Western blot	/	A5316	Sigma-Aldrich

ChIP, Chromatin immunoprecipitation; FSP1, ferroptosis suppressor protein 1; IHC, immunohistochemistry; NRF2, nuclear factor erythroid 2-related factor 2.

Table 3. Primer Sequences

Primer	Sequence
Human FSP1 (ChIP)	Forward: TTCAAAGTTCAAGGCCGTTC Reverse: TGGTCGTCTTCCCGAGTTAC
Human FSP1	Forward: GGAGACAGGGTTCGCCAAAA Reverse: CCCGTGGCCAGGATAAGATG
Human NRF2	Forward: GGTTGCCCACATTCCCAAAT Reverse: AGCAATGAAGACTGGGCTCT
Human KEAP1	Forward: CCTTCAGCTACACCCTGGAG Reverse: AACATGGCCTTGAAGACAGG
Human MAF	Forward: CCCGTCCTCTCCCGAGTTTT Reverse: ACACTGGTAAGTACACGATGCT
Human 18S	Forward: GAGGATGAGGTGGAACGTGT Reverse: AGAAGTGACGCAGCCCTCTA
Mouse Afp	Forward: AAGCAAAAGCCTGAACTGACA Reverse: TCAACTTTGGACCCTCTTCTG
Mouse Gapdh	Forward: GGGTGTGAACCACGAGAAAT Reverse: CCTTCCACAATGCCAAAGTT

Afp, Alpha fetoprotein; ChIP, chromatin immunoprecipitation; FSP1, ferroptosis suppressor protein 1; KEAP1, kelch-like ECH-associated protein 1; MAF, MAF BZIP transcription factor; NRF2, nuclear factor erythroid 2-related factor 2.

following transitions from precursor to product ions: $CoQ_{10}H_2$: m/z 883 >197, CoQ_{10}: m/z 881 >197. Data acquisition and analyses were performed with SCIEX OS software (Sciex Applied Biosystems).

BODIPY 581/591 C_{11} Lipid Peroxidation Detection

Intracellular lipid peroxidation was detected in HCC cells plated on 6-well culture dishes at equal densities. Cells were incubated with 5 μmol/L lipid peroxidation sensor BODIPY 581/591 C_{11} (Invitrogen) at 37 °C for 30 minutes. Cells were washed twice with phosphate buffered saline (PBS) and collected by trypsinization. Pelleted cells were washed with PBS and re-suspended with 2% FBS in PBS. Relative cell staining was determined by the BD LSRFortessa Flow Cytometer (BD Biosciences, San Jose, CA), and results were analyzed using FlowJo Software (BD, Ashland, OR).

Cell Proliferation Assays

HCC cell proliferation rates were determined using 2 different methods: cell counting and Cell Proliferation enzyme-linked immunosorbent assay, BrdU (colorimetric) assay (Roche Diagnostics). For cell counting, HCC cells were plated onto 12-well culture dishes at the original density of 2×10^4 cells per well. Culture media were changed 24 hours after plating cells for pharmacological treatments. Cell counting began 24 hours after treatment. Cells were trypsinized and counted using the TC20 Automated Cell Counter (Bio-Rad Laboratories, Hercules, CA) daily for 4 consecutive days. Uncounted cells were replenished with fresh culture media with appropriate treatments every 24 hours. BrdU colorimetric assay was performed according to the manufacturer's instructions. Briefly, HCC cells of equal density were seeded onto 96-well culture dishes. Pharmacological treatments and BrdU labeling were added 24 hours after cells were plated. Addition of conjugated anti-BrdU antibodies and substrate reactions were performed the next day, and absorbance for each sample was measured on a microplate reader to quantify the cell proliferation.

Animal Experiments

For orthotopic implantation, 1.5×10^6 luciferase-labeled MHCC97L cells were re-suspended in 100% Matrigel (BD Biosciences) and implanted into left lobes of livers of 6- to 8-week-old, male BALB/cAnN-nu (nude) mice. After 6 weeks (42 days) post implantation, tumor-bearing mice were subjected for bioluminescent imaging. The mice were injected intraperitoneally with 100 mg/kg D-Luciferin (Gold Biotechnology, St Louis, MO) then imaged using the PE IVIS Spectrum In Vivo Imaging System (PerkinElmer, Inc, Waltham, MA). Livers and lungs were also extracted for ex vivo imaging.

Table 4. shRNA Target Sequences and Insert Sequences for Luciferase Reporter Assay

shRNA	Target sequence
shNRF2-55	GCTCCTACTGTGATGTGAAAT
shNRF2-94	AGTTTGGGAGGAGCTATTATCC
shKEAP1-57	GCGAATGATCACAGCAATGAA
shKEAP1-76	GTGGCGAATGATCACAGCAAT
shFSP1-23	CGGGCAAGTTTAATGAGGTTT
shFSP1-24	CATTTCTTACTCGGTGACTTT
shMAF-42	TCAGTGGGATACGCCACATTT
shMAF-58	TGGAAGACTACTACTGGATGA
Insert	Sequence
WT	GGGGTCGGGGACCAGCACGAGTGCTGAGTCACGCCCCGCCCGGG
MUT	GGGGTCGGGGACCAGCACGAGTAAAAAAAAACGCCCCGCCCGGG

FSP1, ferroptosis suppressor protein 1; KEAP1, kelch-like ECH-associated protein 1; MAF, MAF BZIP transcription factor; MUT, mutated; NRF2, nuclear factor erythroid 2-related factor 2; shRNA, short hairpin RNA; WT, wild-type.

Table 5. Software Used in scRNA-seq Analysis

Software and algorithms	Source	Identifier
Cell Ranger 3.0.2	10× Genomics	https://www.10xgenomics.com/
Seurat 4.0.2	[66]	https://satijalab.org/seurat/index.html
FastMNN	[67]	https://bioconductor.org/packages/release/bioc/html/scran.html
SingleR	[68]	https://github.com/LTLA/SingleR
Clustree	[69]	https://github.com/lazappi/clustree
REdaS	[70]	http://CRAN.R-project.org/package=REdaS
Complex heatmap	[71]	https://bioconductor.org/packages/ComplexHeatmap/

scRNA-seq, Single-cell RNA sequencing.

For HDTVi, plasmid DNA mixed with sterile saline (0.9% NaCl) at a total volume equivalent to 10% of body weights were injected into the lateral tail vein of 8- to 10-week-old, male C57BL/6N mice within 5 to 7 seconds. A total of 20 μg of CRISPR-Cas9 vector system carrying single guide RNA targeting Keap1 with transposon system carrying c-Myc vector were injected. For HDTVi model, fatty livers were induced by replacing standard diets with HFD 24 hours prior to HDTVi and for the duration of the experiment. FSP1 was inhibited in vivo by daily intraperitoneal injections of 10 mg/kg iFSP1 (Cayman Chemical). Administrations of anti-PD-1 mAb (clone RMP1.14, BioXcell) and anti-PD-L1 mAb (clone 10F.9G2, BioXCell) both began 1-week post HDTVi for 3 weeks, twice weekly by intraperitoneal injection at 10 mg/kg. CD40 agonist (clone FGK45, BioXCell) was administered 2 weeks post HDTVi by intraperitoneal injections at 2.5 mg/kg once per week. To study the effect of iFSP1 on tumor immune infiltrates, HDTVi-induced tumors were harvested 4 weeks post HDTVi for dissociation and histological analysis. To study the therapeutic benefits of combination treatment of iFSP1 and different immunotherapies, mice were sacrificed when they have reached humane endpoint.

All animal procedures performed throughout this study were approved by the Committee on the Use of Live Animals in Teaching and Research of The University of Hong Kong and adhered to the Animals (Control of Experiments) Ordinance of Hong Kong. All animal procedures were performed under the UK Co-ordinating Committee on Cancer Research (UKCCCR) PMID: 9459138 Guidelines for the Welfare of Animals in Experimental Neoplasia to minimize suffering on the animals throughout the experiments.

4-Hydroxynonenal Assay

Quantitation of relative 4-HNE in HCC cells were detected with the Lipid Peroxidation (4-HNE) Assay Kit (Abcam, Cambridge, UK) according to the manufacturer's protocol. Briefly, samples and standards were incubated with anti-4-HNE antibody followed by secondary antibody-HRP conjugate on a 4-HNE conjugate pre-coated plate. After incubation with substrate, enzymatic reactions were stopped with a stop solution, and the absorbance for each sample mixture was measured on a microplate reader at OD 450 nm.

Malondialdehyde Colorimetric Assay

Relative productions of MDA in HCC cells were detected using the Lipid Peroxidation (MDA) Assay kit (Abcam) following the manufacturer's instructions. Briefly, HCC cells were harvested and lysed by homogenization in lysis buffer. Homogenized samples and standards were incubated with thiobarbituric acid. Absorbance measurement of each sample mixture was performed on a microplate reader at OD 532 nm.

Lactate Dehydrogenase Release Measurement

LDH released from damaged HCC cells were measured with Cytotoxicity Detection Kit^{PLUS} (LDH) (Roche Diagnostics) according to the manufacturer's instructions. Briefly, equal densities of HCC cells were plated onto 6-well culture dishes for 24 hours followed by pharmacological treatments where applicable. Conditioned medium from HCC cells were collected, mixed with reaction mixture, and incubated at room temperature in dark for 30 minutes. Reactions in each sample mixture were stopped, and absorbance was measured with microplate reader at OD 490 nm.

Cell Death Analysis

The percentage of dead cells was determined in equal densities of HCC cells plated on 6-well culture dishes for 24 hours followed by pharmacological treatments where applicable. Conditioned medium and HCC cells were collected. The pelleted cells were washed with PBS and resuspended in SYTOX Green dead cell stain (Invitrogen) at room temperature in the dark for 40 minutes. Dead cell percentages were determined by flow cytometry using the BD LSRFortessa Flow Cytometer (BD Biosciences).

Preparation of Bone Marrow-derived Macrophages

Femur and tibia were obtained from 5- to 7-week-old C57/BL6N male mice. Bones were cut at both ends, and bone marrow was flushed out with medium. Bone marrow cells were isolated using Ficoll Paque PLUS (GE Healthcare) according to manufacturer's instruction. Cells were then cultured for 6 days in RPMI 1640 medium supplemented with 25 mM HEPES, 50 μM 2-mercaptoethanol (Sigma-Aldrich), 10% FBS, and 1% P/S in the presence of 20 ng/mL M-CSF (R&D Systems, Minneapolis, MN). More than 90% of

the adherent cells were macrophages as identified by $CD11b^+$ $CD11c^-$ $F4/80^+$.

Phagocytosis Assay

BMMs were seeded at 1×10^5 per well in 12-well plate. Medium was changed the next day. Hepa1-6 cells were treated with iFSP1 at indicated concentration with or without Fer-1 for 24 hours. Hepa1-6 cells with or without treatment were labeled with 2.5μM CTV (Invitrogen) for 20 minutes at 37 °C with mixing at regular intervals. Labeled Hepa1-6 cells were co-cultured with macrophages in 5:1 ratio for 1 hour at 37 °C. Macrophages were harvested and stained for macrophage markers CD11b and F4/80. Phagocytosis events were analyzed by flow cytometry.

Preparation of Single-cell Suspension From Tumor Tissues

Single-cell suspensions from mouse tumors were prepared prior to flow cytometry analysis. Tumors harvested from HCC-bearing mice were cut into fine pieces and transferred to gentleMACS C tube (Milteyni Biotech, Bergisch Gladbach, Germany) containing 10 mL of DMEM/F12 medium (Gibco). Thirty μL of Liberase (2.5 mg/mL; Roche Diagnostics) and 60 μL of DNase I (10 mg/mL; Roche Diagnostics) were added. Samples were further dissociated with GentleMACS Dissociator (Miltenyi Biotech) using the installed programs "h_tumor_01" thrice, "h_tumor_02" twice, and "h_tumor_03" once. Samples were incubated at 37 °C for 15 minutes with regular mixing in between 2 programs. The cell suspensions were then passed through MACS SmartStrainer (Miltenyi Biotech) to remove undigested tissues and cell clumps, followed by centrifugation. The filtered cell suspensions were resuspended with 10 mL ACK lysing buffer (155 mM ammonium chloride, 10 mM potassium bicarbonate, and 0.1 mM EDTA in water) and incubated at room temperature for 5 minutes to lyse the red blood cells. The reaction was stopped by adding 2 volumes (20 mL) of cell staining buffer (0.5% w/v BSA and 2 mM EDTA in PBS). The cell suspensions were filtered again with MACS SmartStrainer and centrifuged. The cell pellets were then resuspended in proper amount of cell staining buffer and were ready for cell counting. All centrifugations were carried at 300 × g for 5 minutes.

Flow Cytometry Analysis

Cells were blocked with anti-mouse CD16/32 Antibody (Biolegend, San Diego, CA) at room temperature for 10 minutes and incubated with fluorochrome-conjugated primary antibody at 4 °C for 30 minutes. Antibodies were used in 1:100 dilution. The cells were washed with 500 μL cell staining buffer once. They were then resuspended in 300 μL cell staining buffer and ready for flow cytometry analysis with the analyzer BD LSRFortessa (BD Biosciences). Primary antibodies used were listed in Table 2. Software FlowJo was used for data analysis.

Single-cell RNA Sequencing

Library preparation. After obtaining single cell suspension from mouse tumors as described above, cells were purified with Dead Cell Removal Kit (Miltenyi Biotech). Purified cells were loaded on the 10× Chromium system and were encapsulated with Single Cell 5' Kit (10× Genomics, Pleasanton, CA). Single-cell gene expression libraries were generated according to manufacturer's protocol.

ScRNA-seq data processing and batch effect correction. The generated scRNA-seq FASTQ files was aligned to mm10 reference by *Cell Ranger 3.0.2*. First, the raw data files of barcodes, features, and matrix were imported and created as a Seurat object. Next, we counted the mitochondrial percentage of each cells, and each data of samples was normalized by the *sctransform* function[64] with the *glmGamPoi* improvement.[65] They were subsequently merged as a Seurat object. Then, the batch effect was corrected by *Fast Mutual Nearest Neighbors (FastMNN)* function. To confirm the correction and visualize the data, the non-linear dimension reduction method tSNE was applied using Seurat function *RunTSNE* with maximum 30 dimensions.

Major cell type annotation and cluster-specific marker gene identification. To annotate each cell with cell type, we first clustered the cells using Seurat function *FindNeighbors* and *FindClusters* with 'resolution' parameter from 0.1 to 1. We applied R-package *Clustree* to establish tree for visualizing the clustering results with different 'resolution' parameter. 'Resolution' of 0.8 was used in subsequent analysis. Next, we used another R-package *SingleR* to annotate the cell types based on the transcriptome of each cell with reference to ImmGen database. Then, we used the Seurat *FindMarkers* function to identify the marker genes of each cluster. We defined the marker genes by: (1) 0.25 increasing logfc and (2) *P*-value less than .05 based on the Wilcoxon rank sum test. After that, the ribosomal and mitochondrial genes were filtered out. We identified 9 major immune cell types (B cells, DCs, macrophages, monocytes, neutrophils, NK cells, pDCs, T cells, and mast cells). The dimensionality of the clustering result was reduced and visualized by tSNE.

Identification of T cell subsets and DC/monocyte/macrophage subsets. To identify the subsets of T cells and DC/monocyte/macrophage, raw data from T cells or monocytes, macrophages, DCs, and pDCs were extracted respectively. A second round of clustering was performed using the same procedures and parameters as the identification of major cell types described above. For T cell subsets, we identified 2 $CD4^+$ T cell populations (CD4-Th and CD4-Tcm) and 4 $CD8^+$ T cell subsets (CD8-Trm, CD8-Proliferating, CD8-Tex and CD8-Tcm). For DC/monocyte/macrophage subsets, we identified 2 macrophage subsets (Mac-1, Mac-2), 3 monocyte subsets (Mono-1, Mono-2, Mono-3), and 4 DC subsets (cDC1, cDC2, cDC3, and pDC). The subset clustering results were mapped to the tSNE plot of major cell types for visualization.

Comparison of cell type proportion in iFSP1 and vehicle-treated tumor. The percentage of cell types in iFSP1 and vehicle-treated tumor was calculated,

respectively, based on the total cell numbers of each sample. The percentage of T cell subsets and DC/monocyte/macrophage subsets were normalized to the total number of cells extracted for the sub-clustering. The 95% confidence intervals were calculated by the *freqCI* function of R-package *REdaS*.

Software used in the scRNA-seq analysis are listed in Table 5.

Statistical Analysis

All statistical analyses were performed using the GraphPad Prism 8.0 or above software (GraphPad Software, Inc, La Jolla, CA). Data were analyzed by the 2-tailed Student *t* test, the log-rank test, or as indicated otherwise. All functional assays are representations of at least 3 independent experiments and are expressed as mean ± standard deviation (SD). *P* values $< .05$ were considered statistically significant.

References

1. Sung H, Ferlay J, Siegel RL, et al. Global Cancer Statistics 2020: GLOBOCAN estimates of incidence and mortality worldwide for 36 cancers in 185 countries. CA Cancer J Clin 2021;71:209–249.
2. Llovet JM, Kelley RK, Villanueva A, et al. Hepatocellular carcinoma. Nat Rev Dis Primers 2021;7:6.
3. Dixon SJ, Lemberg KM, Lamprecht MR, et al. Ferroptosis: an iron-dependent form of nonapoptotic cell death. Cell 2012;149:1060–1072.
4. Jiang X, Stockwell BR, Conrad M. Ferroptosis: mechanisms, biology and role in disease. Nat Rev Mol Cell Biol 2021;22:266–282.
5. Li J, Cao F, Yin HL, et al. Ferroptosis: past, present and future. Cell Death Dis 2020;11:88.
6. Cao JY, Dixon SJ. Mechanisms of ferroptosis. Cell Mol Life Sci 2016;73:2195–2209.
7. Shah R, Shchepinov MS, Pratt DA. Resolving the role of lipoxygenases in the initiation and execution of ferroptosis. ACS Cent Sci 2018;4:387–396.
8. Cheng Y, Zak O, Aisen P, et al. Structure of the human transferrin receptor-transferrin complex. Cell 2004;116:565–576.
9. Hou W, Xie Y, Song X, et al. Autophagy promotes ferroptosis by degradation of ferritin. Autophagy 2016;12:1425–1428.
10. Yang WS, Stockwell BR. Synthetic lethal screening identifies compounds activating iron-dependent, nonapoptotic cell death in oncogenic-RAS-harboring cancer cells. Chem Biol 2008;15:234–245.
11. Seiler A, Schneider M, Forster H, et al. Glutathione peroxidase 4 senses and translates oxidative stress into 12/15-lipoxygenase dependent- and AIF-mediated cell death. Cell Metab 2008;8:237–248.
12. Mao C, Liu X, Zhang Y, et al. DHODH-mediated ferroptosis defence is a targetable vulnerability in cancer. Nature 2021;593:586–590.
13. Quinzii CM, DiMauro S, Hirano M. Human coenzyme Q 10 deficiency. Neurochem Res 2007;32:723–727.
14. Bersuker K, Hendricks JM, Li Z, et al. The CoQ oxidoreductase FSP1 acts parallel to GPX4 to inhibit ferroptosis. Nature 2019;575:688–692.
15. Doll S, Freitas FP, Shah R, et al. FSP1 is a glutathione-independent ferroptosis suppressor. Nature 2019;575:693–698.
16. Zou Y, Palte MJ, Deik AA, et al. A GPX4-dependent cancer cell state underlies the clear-cell morphology and confers sensitivity to ferroptosis. Nat Commun 2019;10:1617.
17. Xu S, Chaudhary O, Rodríguez-Morales P, et al. Uptake of oxidized lipids by the scavenger receptor CD36 promotes lipid peroxidation and dysfunction in CD8+ T cells in tumors. Immunity 2021;54:1561–1577.e7.
18. Green DR, Ferguson T, Zitvogel L, et al. Immunogenic and tolerogenic cell death. Nat Rev Immunol 2009;9:353–363.
19. Garg AD, Nowis D, Golab J, et al. Immunogenic cell death, DAMPs and anticancer therapeutics: an emerging amalgamation. Biochim Biophys Acta 2010;1805:53–71.
20. Savina A, Amigorena S. Phagocytosis and antigen presentation in dendritic cells. Immunol Rev 2007;219:143–156.
21. Acharya D, Li XRL, Heineman RE-S, et al. Complement receptor-mediated phagocytosis induces proinflammatory cytokine production in murine macrophages. Front Immunol 2020;10:3049.
22. Quezada SA, Jarvinen LZ, Lind EF, et al. CD40/CD154 interactions at the interface of tolerance and immunity. Annu Rev Immunol 2004;22:307–328.
23. Murphy WJ, Welniak L, Back T, et al. Synergistic anti-tumor responses after administration of agonistic antibodies to CD40 and IL-2: coordination of dendritic and CD8+ cell responses. J Immunol 2003;170:2727–2733.
24. Beatty GL, Chiorean EG, Fishman MP, et al. CD40 agonists alter tumor stroma and show efficacy against pancreatic carcinoma in mice and humans. Science 2011;331:1612–1616.
25. Hoves S, Ooi C-H, Wolter C, et al. Rapid activation of tumor-associated macrophages boosts preexisting tumor immunity. J Exp Med 2018;215:859–876.
26. Xu IM, Lai RK, Lin SH, et al. Transketolase counteracts oxidative stress to drive cancer development. Proc Natl Acad Sci U S A 2016;113:E725–E734.
27. Lee D, Zhang MS, Tsang FH, et al. Adaptive and constitutive activations of malic enzymes confer liver cancer multi-layered protection against ROS. Hepatology 2021;74:776–796.
28. Lee D, Xu IM, Chiu DK, et al. Folate cycle enzyme MTHFD1L confers metabolic advantages in hepatocellular carcinoma. J Clin Invest 2017;127:1856–1872.
29. Rojo de la Vega M, Chapman E, Zhang DD. NRF2 and the hallmarks of cancer. Cancer Cell 2018;34:21–43.
30. Lee D, Xu IM, Chiu DK, et al. Induction of oxidative stress through inhibition of thioredoxin reductase 1 is an effective therapeutic approach for hepatocellular carcinoma. Hepatology 2019;69:1768–1786.
31. Conrad M, Pratt DA. The chemical basis of ferroptosis. Nat Chem Biol 2019;15:1137–1147.

32. Drijvers JM, Gillis JE, Muijlwijk T, et al. Pharmacologic screening identifies metabolic vulnerabilities of CD8+ T cells. Cancer Immunol Res 2021;9:184–199.
33. Maier B, Leader AM, Chen ST, et al. A conserved dendritic-cell regulatory program limits antitumour immunity. Nature 2020;580:257–262.
34. Cheng S, Li Z, Gao R, et al. A pan-cancer single-cell transcriptional atlas of tumor infiltrating myeloid cells. Cell 2021;184:792–809.
35. Dolma S, Lessnick SL, Hahn WC, et al. Identification of genotype-selective antitumor agents using synthetic lethal chemical screening in engineered human tumor cells. Cancer Cell 2003;3:285–296.
36. Zou Y, Henry WS, Ricq EL, et al. Plasticity of ether lipids promotes ferroptosis susceptibility and evasion. Nature 2020;585:603–608.
37. Viswanathan VS, Ryan MJ, Dhruv HD, et al. Dependency of a therapy-resistant state of cancer cells on a lipid peroxidase pathway. Nature 2017;547:453–457.
38. Ubellacker JM, Tasdogan A, Ramesh V, et al. Lymph protects metastasizing melanoma cells from ferroptosis. Nature 2020;585:113–118.
39. Verma N, Vinik Y, Saroha A, et al. Synthetic lethal combination targeting BET uncovered intrinsic susceptibility of TNBC to ferroptosis. Sci Adv 2020;6:eaba8968.
40. Jiang L, Kon N, Li T, et al. Ferroptosis as a p53-mediated activity during tumour suppression. Nature 2015;520:57–62.
41. Sun X, Niu X, Chen R, et al. Metallothionein-1G facilitates sorafenib resistance through inhibition of ferroptosis. Hepatology 2016;64:488–500.
42. Sun X, Ou Z, Chen R, et al. Activation of the p62-Keap1-NRF2 pathway protects against ferroptosis in hepatocellular carcinoma cells. Hepatology 2016;63:173–184.
43. Efimova I, Catanzaro E, Van der Meeren L, et al. Vaccination with early ferroptotic cancer cells induces efficient antitumor immunity. J Immunother Cancer 2020;8:e001369.
44. Luo X, Gong H-B, Gao H-Y, et al. Oxygenated phosphatidylethanolamine navigates phagocytosis of ferroptotic cells by interacting with TLR2. Cell Death Differ 2021;28:1971–1989.
45. Spranger S, Dai D, Horton B, et al. Tumor-residing Batf3 dendritic cells are required for effector T cell trafficking and adoptive T cell therapy. Cancer Cell 2017;31:711–723.
46. House IG, Savas P, Lai J, et al. Macrophage-derived CXCL9 and CXCL10 are required for antitumor immune responses following immune checkpoint blockade. Clin Cancer Res 2020;26:487–504.
47. Ozga AJ, Chow MT, Luster AD. Chemokines and the immune response to cancer. Immunity 2021;54:859–874.
48. Truman LA, Ford CA, Pasikowska M, et al. CX3CL1/fractalkine is released from apoptotic lymphocytes to stimulate macrophage chemotaxis. Blood 2008;112:5026–5036.
49. Wang W, Green M, Choi JE, et al. CD8(+) T cells regulate tumour ferroptosis during cancer immunotherapy. Nature 2019;569:270–274.
50. Vanmeerbeek I, Sprooten J, De Ruysscher D, et al. Trial watch: chemotherapy-induced immunogenic cell death in immuno-oncology. Oncoimmunology 2020;9:1703449.
51. Jenkins RW, Barbie DA, Flaherty KT. Mechanisms of resistance to immune checkpoint inhibitors. Br J Cancer 2018;118:9–16.
52. Kroemer G, Galluzzi L, Kepp O, et al. Immunogenic cell death in cancer therapy. Annu Rev Immunol 2013;31:51–72.
53. Chen L, Han X. Anti–PD-1/PD-L1 therapy of human cancer: past, present, and future. J Clin Invest 2015;125:3384–3391.
54. Vonderheide RH. CD40 agonist antibodies in cancer immunotherapy. Annu Rev Med 2020;71:47–58.
55. Diggs LP, Ruf B, Ma C, et al. CD40-mediated immune cell activation enhances response to anti-PD-1 in murine intrahepatic cholangiocarcinoma. J Hepatol 2021;74:1145–1154.
56. O'Hara MH, O'Reilly EM, Varadhachary G, et al. CD40 agonistic monoclonal antibody APX005M (sotigalimab) and chemotherapy, with or without nivolumab, for the treatment of metastatic pancreatic adenocarcinoma: an open-label, multicentre, phase 1b study. Lancet Oncol 2021;22:118–131.
57. Jiang Z, Lim S-O, Yan M, et al. TYRO3 induces anti–PD-1/PD-L1 therapy resistance by limiting innate immunity and tumoral ferroptosis. J Clin Invest 2021;131:e139434.
58. Ho WJ, Yarchoan M, Charmsaz S, et al. Multipanel mass cytometry reveals anti–PD-1 therapy–mediated B and T cell compartment remodeling in tumor-draining lymph nodes. JCI Insight 2020;5:e132286.
59. Ma X, Xiao L, Liu L, et al. CD36-mediated ferroptosis dampens intratumoral CD8+ T cell effector function and impairs their antitumor ability. Cell Metabolism 2021;33:1001–1012.e5.
60. Wong CC, Gilkes DM, Zhang H, et al. Hypoxia-inducible factor 1 is a master regulator of breast cancer metastatic niche formation. Proc Natl Acad Sci U S A 2011;108:16369–16374.
61. Wong CC, Tse AP, Huang YP, et al. Lysyl oxidase-like 2 is critical to tumor microenvironment and metastatic niche formation in hepatocellular carcinoma. Hepatology 2014;60:1645–1658.
62. Wong CC, Wong CM, Tung EK, et al. The microRNA miR-139 suppresses metastasis and progression of hepatocellular carcinoma by down-regulating Rho-kinase 2. Gastroenterology 2011;140:322–331.
63. Tang Z, Li S, Guan X, et al. Rapid assessment of the coenzyme Q10 redox state using ultrahigh performance liquid chromatography tandem mass spectrometry. Analyst 2014;139:5600–5604.
64. Hafemeister C, Satija R. Normalization and variance stabilization of single-cell RNA-seq data using regularized negative binomial regression. Genome Biol 2019;20:296.
65. Ahlmann-Eltze C, glmGamPoi Huber W. fitting Gamma-Poisson generalized linear models on single cell count data. Bioinformatics 2021;36:5701–5702.

66. Zhou B, Guo R. Integrative analysis of significant RNA-binding proteins in colorectal cancer metastasis. J Cell Biochem 2018;119:9730–9741.
67. Haghverdi L, Lun ATL, Morgan MD, et al. Batch effects in single-cell RNA-sequencing data are corrected by matching mutual nearest neighbors. Nat Biotechnol 2018;36:421–427.
68. Aran D, Looney AP, Liu L, et al. Reference-based analysis of lung single-cell sequencing reveals a transitional profibrotic macrophage. Nat Immunol 2019;20:163–172.
69. Zappia L, Oshlack A. Clustering trees: a visualization for evaluating clusterings at multiple resolutions. Gigascience 2018;7:giy083.
70. Hatzinger R, Hornik K, Nagel HR. Einführung durch angewandte Statistik. Pearson Deutschland GmbH, 2011.
71. Gu Z, Eils R, Schlesner M. Complex heatmaps reveal patterns and correlations in multidimensional genomic data. Bioinformatics 2016;32:2847–2849.

Received February 4, 2022. Accepted March 1, 2023.

Correspondence
Address correspondence to: Dr Carmen Chak-Lui Wong, T8-010, Block T, Queen Mary Hospital, 102 Pokfulam Road, Pokfulam, Hong Kong. e-mail: carmencl@pathology.hku.hk.

Acknowledgments
The authors thank the Centre for Comparative Medicine Research (CCMR) of The University of Hong Kong in support of our animal experiments, and the School of Biological Sciences, The University of Hong Kong for their technical support in our mass spectrometry experiment. We also thank the Genomics and Bioinformatics Cores, and the Imaging and Flow Cytometry Core of the Centre for PanorOmic Sciences (CPOS) from the Li Ka Shing Faculty of Medicine, The University of Hong Kong for their technical support in our single-cell RNA sequencing and in vivo imaging experiments, respectively.

CRediT Authorship Contributions

Jacinth Wing-Sum Cheu (Conceptualization: Lead; Data curation: Lead; Formal analysis: Lead; Investigation: Lead; Methodology: Lead; Visualization: Lead; Writing – original draft: Lead; Writing – review & editing: Lead)

Derek Lee (Conceptualization: Lead; Data curation: Lead; Formal analysis: Lead; Investigation: Lead; Methodology: Lead; Visualization: Lead; Writing – original draft: Lead; Writing – review & editing: Lead)

Qidong Li (Conceptualization: Lead; Data curation: Lead; Formal analysis: Lead; Investigation: Lead; Methodology: Lead; Validation: Lead; Writing – original draft: Lead; Writing – review & editing: Lead)

Chi Ching Goh (Conceptualization: Supporting; Data curation: Supporting; Formal analysis: Supporting; Investigation: Supporting; Methodology: Supporting)

Macus Hao-Ran Bao (Data curation: Supporting; Investigation: Supporting; Methodology: Supporting)

Vincent Wai-Hin Yuen (Data curation: Supporting; Investigation: Supporting)

Misty Shuo Zhang (Data curation: Supporting; Investigation: Supporting)

Chunxue Yang (Data curation: Supporting; Investigation: Supporting)

Cerise Yuen-Ki Chan (Data curation: Supporting; Investigation: Supporting)

Aki Pui-Wah Tse (Data curation: Supporting; Investigation: Supporting)

Grace Fu-Wan Sit (Data curation: Supporting; Investigation: Supporting)

Cindy Xinqi Liu (Data curation: Supporting; Investigation: Supporting)

Irene Oi-Lin Ng (Funding acquisition: Lead; Clinical sample provision: Lead)

Chun-Ming Wong (Conceptualization: Lead; Supervision: Supporting; Writing – review & editing: Lead)

Carmen Chak-Lui Wong (Conceptualization: Lead; Funding acquisition: Lead; Supervision: Lead; Validation: Lead; Writing – original draft: Lead; Writing – review & editing: Lead)

Conflicts of interest
The authors disclose no conflicts.

Funding
The study was supported by the Hong Kong Research Grant Council (RGC) General Research Fund (17112521), RGC Theme-Based Research Fund (T12-716/22-R), and Centre for Oncology and Immunology under the Health@InnoHK initiative funded by the Innovation and Technology Commission, The Government of Hong Kong, SAR, China. Carmen Chak-Lui Wong is a recipient of the Croucher Innovation Award, The University of Hong Kong Outstanding Young Researcher Award, and National Natural Science Foundation of China (NSFC) Excellent Young Scientists Fund (Hong Kong and Macau) (82022077).